Basic Notions and Applications of the Augmented Spherical Wave Method

VOLKER EYERT

Institut für Physik, Universität Augsburg, Universitätsstraße 1, D-86135 Augsburg, Germany

ABSTRACT: The basic ideas of modern band theory and the functionality of state of the art calculational schemes are illustrated with the augmented spherical wave (ASW) method. Our description includes a short review of the underlying theory as well as a derivation of the most important formulas. We explain some steps toward the computational implementation and discuss aspects of practical application. Finally, the capabilities offered by the ASW method are demonstrated by an investigation of the electronic structure of FeS_2, which belongs to the increasingly exciting class of pyrite-type transition metal dichalcogenides.   © 2000 John Wiley & Sons, Inc. Int J Quant Chem 77: 1007–1031, 2000

Key words: augmented spherical wave; atom-centered basis functions; multiple scattering theory; density functional theory; FeS_2

Introduction

First-principles investigations have been established as an important branch of condensed matter physics and solid state chemistry in the past decades. In particular, the last 10 years of the twentieth century have seen an increasing distribution of density-functional-based computational methods, which allow for a detailed understanding of electronic, magnetic, and structural properties of condensed matter. Nowadays these methods can be easily applied to rather complex systems and thus enable the investigation of "real materials." For this reason, band structure methods have left the realm of only a few specialists and have become a standard tool of materials science in universities, research institutes, and industry. Although this success is strongly related to the incredible growth of computer power and the advent of efficient computer architectures, e.g., parallel machines, the base was laid many years ago by a few very important simplifications, which had a great influence on solid state theory in general and on the progress made in electronic structure calculations in particular.

First of all, modern solid state physics has benefited much from Bloch's 1929 theorem, which grew out of early X-ray diffraction studies and allowed focusing on a small unit cell with only a few atoms instead of the full solid with an order of 10^{23} atoms [1]. In this way it was possible for the first time to cast the problem connected with the macroscopic crystal into a tractable form. Only two years before, Born and Oppenheimer had proposed the adiabatic

approximation, which enables an effective decoupling of the electronic and lattice degrees of freedom and, hence, allows the ionic dynamics to be ignored in many cases, where only the electronic structure was of interest [2]. One decade later, Slater invented the so-called muffin-tin approximation, which laid ground for a very efficient determination of basis functions for use in a variational procedure [3]. The introduction of density functional theory and the local density approximation in the mid-sixties by Hohenberg, Kohn, and Sham marked a milestone [4, 5], that has been described in numerous textbooks (see, e.g., [6–14]) and, laying the basis for modern materials science, was honored by awarding the 1998 Nobel Prize in Chemistry to Walter Kohn. Other important steps were the foundation of the pseudopotential methods by Herring, Phillips, and others [15–17] as well as the concept of the so-called linear methods introduced by Andersen in the middle of the seventies [18, 19], which enabled performing first-principles calculations for unit cells of so far inaccessible size and, hence, furthered our understanding of materials considerably. Finally, Car and Parrinello, who introduced first-principles molecular dynamics, made the simultaneous ab initio investigation of electronic and ionic properties accessible [20].

Taken together, all these ideas laid the groundwork, for modern electronic structure calculations, but still gave enough freedom for the development of different calculational schemes, which have evolved in the last years. In the present contribution, we will explain the major ingredients (which are common to most schemes) of the augmented spherical wave (ASW) method, which, within the framework of density functional theory and the local density approximation, allows for both a conceptually simple and a fast calculation of the electronic properties fo solids [21–23]. The ASW method has been applied to a large variety of materials (see, e.g., [22, 24, 25] and references therein) and, due to its very small basis set size, is particularly useful for large systems. (A full list of publications and theses related to the augmented spherical wave method can be accessed via the World Wide Web from the home page of the author, http://www.physik.uni-augsburg.de/~eyert/.)

This article is organized as follows: After a short overview on density functional theory-based electronic structure calculational schemes in the next section, we proceed with a detailed description of the ASW method in subsequent sections. Although we will also touch on computational aspects of the method, for more detailed information we refer the reader to recent publications of the author [24, 26, 27]. In the last part of this article, the capabilities of the method are elucidated via an application to iron pyrite, which has been the subject of recent renewed interest. For a comprehensive overview on uranium ternary intermetallic systems as studied by ASW first-principles calculations, we refer, in addition, to the article by Matar [28] contained in this volume.

Methods for Electronic Structure Calculations

The practical virtue of density functional theory stems, to a large part, from the second theorem of Hohenberg and Kohn, which established a variational principle for the total ground state energy [14]. This suggests expansion of the single-particle wave function in a suitable set of basis functions,

$$\psi_{\mathbf{k}}(\mathbf{r}) = \sum_i c_i(\mathbf{k})\chi_{\mathbf{k}i}(\mathbf{r}), \qquad (1)$$

and minimization of the total energy with respect to the coefficients $c_i(\mathbf{k})$. For simplicity in writing, we have included the band index, which labels different states at a particular $\mathbf{k}$ point, in the $\mathbf{k}$ index. Of course, the basis functions themselves may be parametrically dependent and, hence, offer some freedom for variation. However, for the present purpose, we assume them to be fixed. The variation of the total energy with respect to the coefficients is easily written down as

$$\sum_{\mathbf{k}i}\left[\frac{\delta E[\rho]}{\delta c_i^*(\mathbf{k})} + E(\mathbf{k})\frac{\delta(N - \int \rho(\mathbf{r})\,d^3\mathbf{r})}{\delta c_i^*(\mathbf{k})}\right]\delta c_i^*(\mathbf{k}) = 0, \quad (2)$$

where $E[\rho]$ is the total energy provided by density functional theory and the second term in square brackets ensures conservation of the total electron number. Since all the coefficients $c_i(\mathbf{k})$ are independent of each other, the expression in square brackets in Eq. (2) must vanish for each $c_i(\mathbf{k})$. We combine Eq. (2) with the standard expressions for the electron density, the kinetic energy, and the exchange–correlation potential as supplied by density functional theory,

$$\rho(\mathbf{r}) = \sum_{\mathbf{k}}\left|\psi_{\mathbf{k}}(\mathbf{r})\right|^2\Theta\!\left(E_F - E(\mathbf{k})\right), \qquad (3)$$

$$T_0[\rho] = \sum_{\mathbf{k}}\langle\psi_{\mathbf{k}}(\mathbf{r})|-\nabla^2|\psi_{\mathbf{k}}(\mathbf{r})\rangle\Theta\!\left(E_F - E(\mathbf{k})\right), \quad (4)$$

and

$$v_{xc}(\mathbf{r}) = \frac{\delta E_{xc}[\rho]}{\delta \rho(\mathbf{r})}, \tag{5}$$

where the Heaviside step function $\Theta(E_F - E(\mathbf{k}))$ restricts the sums to the occupied states, and arrive at the secular equation

$$\sum_j [\langle \chi_{\mathbf{k}i}(\mathbf{r})| -\Delta + v_{eff}(\mathbf{r}) | \chi_{\mathbf{k}j}(\mathbf{r}) \rangle$$
$$- E(\mathbf{k}) \langle \chi_{\mathbf{k}i}(\mathbf{r}) | \chi_{\mathbf{k}j}(\mathbf{r}) \rangle] c_j(\mathbf{k}) = 0. \tag{6}$$

Here we have used the Kohn–Sham expression of the single particle Hamiltonian, which, in addition to the kinetic energy operator, contains the effective single-particle potential. So that the linear equation system has nontrivial solutions, the determinant of the secular matrix, i.e., of the matrix in square brackets in Eq. (6), must vanish and the single-particle energies arise as its roots.

Although the approach (1) is conceptually clear, it still leaves some freedom for different choices of basis functions in practice. Of course, the set $\{\chi_{\mathbf{k}i}(\mathbf{r})\}$ is finite and thus we cannot expect it to be complete. In addition, the basis functions are not necessarily orthogonal. As a consequence, the actual shape of the basis functions is an important factor, which governs the size of the basis set, the Hilbert space sampled by the variational procedure, and, finally, the effort to solve the secular equation (6). Obviously, a good choice consists of basis functions $\chi_{\mathbf{k}i}(\mathbf{r})$, which resemble the final wave function $\psi_{\mathbf{k}}(\mathbf{r})$ quite well. In this case, the latter would have a large portion within the Hilbert space spanned by the basis function for only a small set $\{\chi_{\mathbf{k}i}(\mathbf{r})\}$ and the dimension of the secular matrix would be rather small.

At a first glance, for crystals the canonical set of basis functions seems to be a plane wave basis,

$$\chi_{\mathbf{k}\nu}(\mathbf{r}) = e^{i(\mathbf{k}+\mathbf{K}_\nu)\mathbf{r}}, \tag{7}$$

which offers the additional advantage of being orthogonal. However, plane waves are not really a good choice for the following physical reasons. Since the crystal potential arises from a superposition of atomic potentials, near the atomic centers the valence electrons are subject to the strong bare nuclear Coulomb potential, which behaves like $-Ze^2/r$. In contrast, far away from the nuclei the potential changes to $-Z_\nu e^2/r$, where Z_ν is the valence charge. This is due to electrostatic screening by the core electrons. Finally, in the region between the atoms the potential becomes rather flat because of crystalline periodicity. Thus the wave function

shows large oscillations near the nuclei and is rather smooth in the region far away from the atomic cores. As a consequence, to describe such a wave function by a plane wave basis, we would need a huge number of functions. Indeed, as Heine demonstrated, this could well lead to a secular matrix with a rank on the order 10^6 [29].

Obviously, the basis functions have to be adapted to better account for the details of the crystal potential. There exist mainly two approaches to do so, one being the pseudopotential (PP) concept, which traces back to Herring's orthogonalized plane wave (OPW) method [15] (see also [30, 31]). In the latter scheme one starts out from plane waves as basis functions, but orthogonalizes them to the core states from the very beginning. We write

$$\chi_{\mathbf{k}\nu}(\mathbf{r}) = |\mathbf{k} + \mathbf{K}_\nu\rangle - \sum |\phi_c\rangle \langle \phi_c | \mathbf{k} + \mathbf{K}_\nu \rangle, \tag{8}$$

where $|\mathbf{K}_\nu\rangle$ and $|\phi_c\rangle$ denote a plane wave and the Bloch sum of the core states, respectively. Each orthogonalized plane wave consists of a long range term and a part that shows strong oscillations in the core regions. Hence, the appropriate shape near the nuclei is built in and already a moderate number of OPWs are sufficient for a good description of the wave function. Starting out from Herring's scheme, Phillips and Kleinman, as well as Antoncik later on, reformulated the orthogonalization to the core states in terms of an additional potential seen by the valence electrons and thereby they laid the groundwork for pseudopotential theory [16, 17, 32], which, in subsequent years, was refined by the introduction of norm-conserving pseudopotentials (see, e.g., [33–35]). Recently, Vanderbilt developed ultrasoft pseudopotentials, which even allowed treatment of transition metal atoms [36]. For details, we refer the reader to the literature (see, e.g., [29, 37–39] as well as references therein).

The second approach mentioned above is based on Slater's muffin-tin approximation (MTA) [3] (see also [40]). In this approximation the crystal potential is restricted to an idealized shape, i.e., it is assumed to be spherically symmetric within (nonoverlapping) muffin-tin spheres and constant in the remaining, interstitial region. The wave function in the latter region is well described by plane waves and inside the muffin-tin spheres the radial Schrödinger equation can be solved numerically with the actual potential. By matching the radial functions continuously to the plane waves at the sphere boundary, we arrive at a single basis function, which, due to the way it was constructed, is called an augmented plane wave (APW). The APW method has been de-

cribed in much detail in the book by Loucks, to which the reader is referred [41].

The inaccuracy of the basis functions as constructed within the muffin-tin approximation is cured to a large extent by the variational principle, which is used to determine the wave function. To be specific, we may evaluate the basis functions with the MTA, but may incorporate the full, unrestricted potential in the Hamiltonian entering the secular matrix. Thereby we will arrive at a very accurate, so-called full potential method, which even allows for evaluation of elastic properties. This is due to the fact that the muffin-tin potential constitutes a good approximation to the full potential—a fact that allowed only for Slater's important step—and thus the basis functions very much resemble the final wave function.

Although the use of plane waves is a natural consequence of Bloch's theorem and, in addition, offers the advantage of mathematical simplicity, doubts come up if we prefer a chemist's point of view and put more emphasis on the single atoms rather than the periodic array they form. In this case we will opt for spherical waves, which are products of spherical harmonics and spherical Hankel, Neumann, or Bessel functions, and, like plane waves, solve Schrödinger's equation with a constant potential. By augmenting the spherical waves with numerical solutions of the radial equation inside the muffin-tin spheres in the same manner as in the APW method, we arrive at the Korringa–Kohn–Rostoker (KKR) method, even though this method was developed originally in a much different way [42, 43] (see also [44–46]). Compared to methods based on plane waves, spherical waves offer the particular advantage of leading to a smaller secular matix, usually an order of magnitude less. Moreover, since spherical waves are much better adapted to notions from atomic physics or chemistry, they allow for a more natural interpretation of the results.

The radial solutions of Schrödinger's equations inside the muffin-tin spheres appearing in both the APW and the KKR method are energy-dependent functions and so are the basis functions. Although they make calculations of very high accuracy feasible, this means a great computational effort since with energy-dependent basis functions the electronic energies $E(\mathbf{k})$ can be accessed only via time-consuming root tracing. In contrast, were it not for the energy dependence, we would end up with the generalized eigenproblem (6), which can be solved much faster.

It was thus a great success when Andersen observed that the energy dependence within the APW and the KKR method actually is rather weak in the energy region of interest for the valence electrons [18, 19]. Using this as a starting point, Andersen modelled the weak energy dependence by a Taylor series expansion, where only the first two terms are kept. In doing so, he arrived at the so-called linear methods. In particular, Andersen devised the linear augmented plane wave (LAPW) and the linear muffin-tin orbital (LMTO) methods as linearized counterparts of the APW and the KKR method (see, e.g., [47–52]). By combining Andersen's idea to linearize the energy dependence of the wave function with the renormalized-atom description of solids as presented by Watson, Ehrenreich, Hodges, and Gelatt [53–55], Williams, Kübler, and Gelatt later developed the augmented spherical wave (ASW) method [21], wich will be discussed in detail below. Altogether, besides being much faster than the classical schemes, the linear methods enabled, for the first time, calculations on much more realistic and complex systems. In this way, Andersen opened the door to an unexpected understanding of the physical as well as the chemical properties of condensed matter.

Another approach to circumvent the problem of energy-dependent basis functions is provided by the linear combination of atomic orbitals (LCAO) methods, which uses products of spherical harmonics and analytically known radial functions. Several schemes along this line have been proposed, of which we just mention the work of Wang and Callaway [56] as well as of Eschrig [57].

Despite the great success of density functional theory-based electronic structure calculations it was not until the mid-eighties that a simultaneous minimization of the electronic and ionic energies could be performed. Indeed, any band calculation scheme, if accurate enough, in principle allows determination of the forces acting on the atoms,

$$\mathbf{F}_\mu = -\nabla_{\mathbf{R}_\mu} E\big(\{\psi_{\mathbf{k}}, \mathbf{R}_\mu\}\big), \qquad (9)$$

which could be used to optimize the atomic positions. However, such an approach is not very efficient since it requires in each step a renewed self-consistent calculation of the electronic structure before the atoms can be moved.

A substantial improvement was made by Car and Parrinello, who introduced a new approach to first-principles molecular dynamics by treating the electronic wave functions as dynamical variables [20]. To do so, Car and Parrinello started out

from the Lagrangian

$$L = \bar{\mu} \sum_{\mathbf{k}} \int d^3\mathbf{r} \left| \dot{\psi}_{\mathbf{k}}(\mathbf{r}, t) \right|^2$$

$$+ \frac{1}{2} \sum_{\mu} M_{\mu} \left[\dot{\mathbf{R}}_{\mu} \right]^2 - E(\{\psi_{\mathbf{k}}, \mathbf{R}_{\mu}\})$$

$$+ \sum_{\mathbf{k}\mathbf{k}'} \left\{ \int d^3\mathbf{r}\, \psi_{\mathbf{k}}^*(\mathbf{r}, t) \psi_{\mathbf{k}'}(\mathbf{r}, t) - \delta_{\mathbf{k}\mathbf{k}'} \right\} \lambda_{\mathbf{k}\mathbf{k}'}, \quad (10)$$

where the overdot as usual denotes d/dt, and M_{μ} and $\mathbf{R}_{\mu}$ are the ionic masses and positions, respectively. Moreover, $\bar{\mu}$ is a fictitious mass associated with the electronic wave functions, which are assumed to follow an artificial classical dynamics. Note that the total energy in this context plays the role of a potential term. Finally, the last term on the right-hand side of Eq. (10) ensures orthonormality of the electronic wave functions and is coupled via a Langrange multiplier. Note again that the band index is included in the $\mathbf{k}$ index.

Following the laws of classical mechanics, we easily derive from the Lagrangian (10) the equations of motions for the electronic wave functions,

$$\bar{\mu} \ddot{\psi}_{\mathbf{k}}(\mathbf{r}, t) = -\left[-\Delta + v_{\text{eff}}(\mathbf{r}) \right] \psi_{\mathbf{k}}(\mathbf{r}, t)$$

$$+ \sum_{\mathbf{k}'} \lambda_{\mathbf{k}\mathbf{k}'} \psi_{\mathbf{k}'}(\mathbf{r}, t), \quad (11)$$

and for the ionic motion

$$M_{\mu} \ddot{\mathbf{R}}_{\mu} = -\nabla_{\mathbf{R}_{\mu}} E(\{\psi_{\mathbf{k}}, \mathbf{R}_{\mu}\}). \quad (12)$$

Note that in the stationary state the left-hand side of Eq. (11) vanishes, while the right-hand side reduces to the usual Kohn–Sham equation except for a possible unitary transformation.

The last decade has witnessed numerous work to implement and improve different first-principles molecular dynamics schemes, the discussion of which again would be far beyond the scope of this article (recent references are, for instance, [58, 59]). Nevertheless, the idea of Car and Parrinello, in addition to leading to first-principles molecular dynamics, had a large influence also on the electronic problem by itself since it revealed a way to determine the electronic wave function by direct minimization instead of solving the secular equation. This likewise marked a starting point for new developments [58].

After this more general overview, we will focus in the following sections on the augmented spherical wave (ASW) method, which combines the advantages of a linear method with the benefits of the minimal basis set arising from the use of spherical waves. It thus offers the aforementioned advantages to allow for investigations of rather complex compounds as well as a rather simple interpretation of the calculated electronic properties in terms of atomic orbitals.

Our discussion of the ASW method proceeds along the following lines: We start out by defining the ASW basis functions. After this, an efficient way to evaluate the elements of the secular matrix is given. From the solution of the thus defined eigenproblem, we get the expansion coefficients of the wave function (1) in terms of the basis functions. This in turn enables calculation of the charge density, magnetization, total energy, and effective single-particle potential, which latter closes the self-consistency cycle.

Construction of Augmented Spherical Wave Basis Functions

The standard augmented spherical wave method relies on Slater's MTA, which replaces the full crystal potential by its spherical symmetric average within nonoverlapping atomic spheres. In the remaining interstitial region the potential is flat and, hence, approximated by a constant, the muffin-tin zero v_{MTZ}. The effective single-particle potential entering Schrödinger's equation,

$$\left[-\Delta + v_{\sigma}(\mathbf{r}) - \varepsilon \right] \psi_{\sigma}(\varepsilon, \mathbf{r}) = 0, \quad (13)$$

thus has the form

$$v_{\sigma}^{\text{MT}}(\mathbf{r}) = v_{\text{MTZ}} \Theta_I + \sum_{\mu i} v_{i\sigma}^{\text{MT}}(\mathbf{r}_{\mu i}) \Theta_{\mu i}, \quad (14)$$

where $v_{\sigma}(\mathbf{r})$ denotes the spin-dependent, effective single-particle potential, σ is the spin index, and $\psi_{\sigma}(\varepsilon, \mathbf{r})$ a spinor component of the wave function. In Eq. (14) we used the definitions

$$\mathbf{r}_{\mu i} := \mathbf{r} - \mathbf{R}_{\mu i} \quad \text{and} \quad \mathbf{R}_{\mu i} := \mathbf{R}_{\mu} + \boldsymbol{\tau}_i, \quad (15)$$

where $\mathbf{R}_{\mu}$ is a lattice vector and τ_i is the position of the nucleus i within the unit cell. The step functions Θ_I and $\Theta_{\mu i}$ limit the range of the functions attached to them to the interstitial region and the atomic sphere of radius S_i centered at site $\mathbf{R}_{\mu i}$, respectively.

Within the MTA the choice of the atomic sphere radii is restricted by the requirement that the spheres must not overlap. A somehow different standpoint is taken by the atomic sphere approximation (ASA), which requires the sum of the atomic

sphere volumes to equal the cell volume, i.e.,

$$\sum_i \Omega_i := \sum_i \frac{4\pi}{3} S_i^3 \stackrel{!}{=} \Omega_c. \qquad (16)$$

Here Ω_i and Ω_c denote the volumes of the atomic sphere i and the unit cell, respectively. Due to this restriction, only the ratios of the sphere radii may still be varied. The atomic sphere approximation was invented by Andersen to formally eliminate the interstitial region. This was a natural consequence of the linearization of the energy dependence of the wave function, which keeps the first two terms of the respective Taylor expansion within the atomic spheres, while, in combination with the ASA, even the linear term may be omitted in the interstitial region. In the following discussion, we will opt for the ASA, but still want to develop the theory on very general grounds as long as possible. Thus we keep the muffin-tin form (14) for the potential without fixing the radii of the atomic spheres.

Using the muffin-tin form of the effective single-particle potential, we construct the basis functions in the following way: First Schrödinger's equation is solved separately in the atomic spheres and the interstitial region. The resulting partial waves are then matched continuously and differentiably at the sphere boundaries to form a single basis function, an augmented spherical wave. Hence, the basis functions must obey Schrödinger's equation with the muffin-tin potential (14),

$$\left[-\Delta + v_\sigma^{\mathrm{MT}}(\mathbf{r}) - \varepsilon \right] \phi_\sigma(\varepsilon, \mathbf{r}) = 0, \qquad (17)$$

separately in the interstitial and the atomic spheres.

In the interstitial region we combine Eqs. (14) and (17) and arrive at Helmholtz's equation

$$\left[-\Delta - \kappa^2 \right] \phi_\sigma\left(\kappa^2, \mathbf{r}\right) = 0 \qquad (18)$$

with

$$\kappa^2 = \varepsilon - v_{\mathrm{MTZ}}. \qquad (19)$$

As already outlined before, the ASW method uses the spherical wave solutions of this differential equation, which are atom-centered products of spherical harmonics and radial functions. The latter are solutions of the free particle radial Schrödinger equation for energy κ^2 and, hence, are well known as spherical Bessel, Neumann, or Hankel functions. Note that the singularities of the latter two functions do not come into play here since we are interested in solutions for the interstitial region only.

In contrast to the KKR method, the energy dependence of the wave function is suppressed in the ASW method, which uses radial functions for only

a fixed value of κ^2. This value should be somewhere in the region of interest, usually between -1 Ry and $+1$ Ry. While in the KKR method spherical Neumann functions are chosen as the interstitial part of the basis functions, the ASW method employs spherical Neumann and Hankel functions for positive and negative values of κ^2, respectively. The interstitial energy κ^2 usually is set to -0.015 Ry. Still, the albeit small limitations due to the energy linearization may be cured by employing a so-called multiple-κ set, which takes envelope functions with two or three different values of the interstitial energy into account. Although this is not necessary within the ASA, it will be important for MTA-based full potential methods. For this reason we include the energy parameter in the subsequent description. Nevertheless, since usually only negative κ^2 are considered, we will from now on concentrate on the negative energy case and, hence, on the use of Hankel-type envelope functions.

To be specific, we define the interstitial part of the ASW basis function by

$$H_{L\kappa\sigma}^\infty(\mathbf{r}_{\mu i})\Theta_I := H_{L\kappa}^i(\mathbf{r}_{\mu i}) := H_{L\kappa}(\mathbf{r}_{\mu i})\Theta_I, \qquad (20)$$

where $H_{L\kappa}$ is the envelope function given by

$$H_{L\kappa}(\mathbf{r}_{\mu i}) := i\kappa^{l+1} h_l^{(1)}(\kappa \mathbf{r}_{\mu i}) Y_L(\hat{\mathbf{r}}_{\mu i}). \qquad (21)$$

In somewhat lax notation the latter, too, is sometimes referred to as the Hankel function. In Eq. (21), $h_l^{(1)}(\kappa r_{\mu i})$ denotes the spherical Hankel function in the notation of Abramowitz and Stegun [60, Chap. 10]. The index $L = (l, m)$ is composed of the angular momentum and magnetic quantum numbers, $Y_L(\hat{\mathbf{r}}_{\mu i})$ denotes a spherical (or cubic) harmonic, and the prefactors finally serve the purpose of cancelling the leading κ dimension and making the radial functions real for negative energies κ^2.

Next, we turn to the regions inside the atomic spheres, where the potential shows all the intraatomic details and, hence, solving Schrödinger's equation is much more complicated. However, the reduction of the full crystal potential to its spherical symmetric average inside the atomic spheres due to the muffin-tin approximation allows for a separation of Schrödinger's equation into an angular and a radial part. The latter furthermore is subject to the conditions of continuous and differentiable matching to the interstitial basis function.

We first concentrate on that single atomic sphere where the spherical wave is centered. In this so-called on-center sphere we use the spherical symmetry and arrive at the following intraatomic basis

function, the augmented Hankel function:

$$H_{L\kappa\sigma}^{\infty}(\mathbf{r}_{\mu i})\Theta_{\mu i} := \tilde{H}_{L\kappa\sigma}(\mathbf{r}_{\mu i}) := \tilde{h}_{l\kappa\sigma}(\mathbf{r}_{\mu i})Y_L(\hat{\mathbf{r}}_{\mu i})\Theta_{\mu i}. \quad (22)$$

Its radial part obeys the radial Schrödinger equation

$$\left[-\frac{1}{r_{\mu i}}\frac{\partial^2}{\partial r_{\mu i}^2}r_{\mu i} + \frac{l(l+1)}{r_{\mu i}^2} + v_{i\sigma}^{\mathrm{MT}}(r_{\mu i}) - E_{l\kappa i\sigma}^{(H)} \right]$$
$$\times \tilde{h}_{l\kappa\sigma}(r_{\mu i}) = 0. \quad (23)$$

The numerical solution of this differential equation as well as the determination of the Hankel energy $E_{l\kappa i\sigma}^{(H)}$ is subject to three boundary conditions, namely the regularity of the radial function $\tilde{h}_{l\kappa\sigma}(r_{\mu i})$ at its origin as well as the continuous and differentiable matching at the sphere boundary,

$$\left[\left(\frac{\partial}{\partial \mathbf{r}_{\mu i}}\right)^n \left(\tilde{h}_{l\sigma}(\mathbf{r}_{\mu i}) - i\kappa^{l+1}h_l^{(1)}(\kappa \mathbf{r}_{\mu i})\right) \right]_{r_{\mu i}=S_i} = 0,$$
$$n = 0,1. \quad (24)$$

Note that, for simplicity in writing, we have omitted the principal quantum number in Eq. (23). This is motivated by the observation that in many cases it is sufficient to take into account only one valence state per atom and angular momentum, and that all the lower lying core states do not extend beyond the atomic sphere.

By now we have augmented the spherical wave inside the on-center sphere. In all other atomic spheres of the crystal, which are centered at $\mathbf{R}_{\nu j} \neq \mathbf{R}_{\mu i}$ and referred to as the off-center spheres, the situation is different. Inside these spheres, the envelope function lacks spherical symmetry relative to the center of the respective sphere, $\mathbf{R}_{\nu j}$. For this reason we first apply the expansion theorem for the envelope functions, which allows us to expand the Hankel function defined in Eq. (21) and centered at site $\mathbf{R}_{\mu i}$ in terms of Bessel functions centered at $\mathbf{R}_{\nu j}$,

$$H_{L\kappa}(\mathbf{r}_{\mu i}) = \sum_{L'} J_{L'\kappa}(\mathbf{r}_{\nu j})B_{L'L\kappa}(\mathbf{R}_{\nu j} - \mathbf{R}_{\mu i}). \quad (25)$$

It is valid for all vectors $\mathbf{r}$, which fulfil $|\mathbf{r}_{\nu j}| < |\mathbf{R}_{\nu j} - \mathbf{R}_{\mu i}|$, and thus for all $\mathbf{r}$ lying within a sphere of radius equal to the distance between the two centers and centered at $\mathbf{R}_{\nu j}$. The Bessel function

$$J_{L'\kappa}(\mathbf{r}_{\nu j}) := \kappa^{-l'}j_{l'}(\kappa r_{\nu j})Y_{L'}(\hat{\mathbf{r}}_{\nu j}), \quad (26)$$

like the Hankel function given by Eq. (21), is a solution of Helmholtz's Eq. (18). $j_{l'}(\kappa r_{\nu j})$ denotes a spherical Bessel function and the prefactor again was introduced to cancel the leading κ dimension and to make the radial part real for any value of κ^2.

The expansion coefficients entering Eq. (25) are the so-called structure constants, which are related to those of the KKR method. Their calculation as well as the proof of the expansion theorem has been given in full detail in [22, 23]. Here we present only the result

$$B_{L'L\kappa}(\mathbf{R}_{\nu j} - \mathbf{R}_{\mu i}) = 4\pi \sum_{L''} i^{l-l'-l''}\kappa^{l+l'-l''}c_{LL'L''}$$
$$\times H_{L''\kappa}(\mathbf{R}_{\nu j} - \mathbf{R}_{\mu i}), \quad (27)$$

which is valid for $\mathbf{R}_{\nu j} \neq \mathbf{R}_{\mu i}$ and where

$$c_{LL'L''} = \int d^2\hat{\mathbf{r}}\, Y_L^*(\hat{\mathbf{r}})Y_{L'}(\hat{\mathbf{r}})Y_{L''}(\hat{\mathbf{r}}) \quad (28)$$

denotes the Gaunt coefficient.

With the expansion theorem (25) at hand we are ready to augment the spherical wave in the off-center spheres since the Bessel functions given by Eq. (26) are centered at the corresponding atomic sites and thus reflect the spherical symmetry relative to these sites. The basis function in the off-center sphere centered at $\mathbf{R}_{\nu j}$ is thus written in terms of augmented Bessel functions

$$\tilde{J}_{L'\kappa\sigma}(\mathbf{r}_{\nu j}) := \tilde{j}_{l'\kappa\sigma}(r_{\nu j})Y_{L'}(\hat{\mathbf{r}}_{\nu j})\Theta_{\nu j}. \quad (29)$$

Their radial parts have to obey the radial Schrödinger equation

$$\left[-\frac{1}{r_{\nu j}}\frac{\partial^2}{\partial r_{\nu j}^2}r_{\nu j} + \frac{l'(l'+1)}{r_{\nu j}^2} + v_{j\sigma}^{\mathrm{MT}}(r_{\nu j}) - E_{l'\kappa j\sigma}^{(J)} \right]$$
$$\times \tilde{j}_{l'\kappa\sigma}(r_{\nu j}) = 0. \quad (30)$$

As for the augmented Hankel function, the numerical solution of this differential equation as well as the determination of the Bessel energy $E_{l'\kappa j\sigma}^{(J)}$ is subject to the conditions of the regularity of the radial function $\tilde{j}_{l'\kappa\sigma}(r_{\nu j})$ at the origin and the continuous and differentiable matching at the sphere boundary,

$$\left[\left(\frac{\partial}{\partial r_{\nu j}}\right)^n \left(\tilde{j}_{l'\kappa\sigma}(r_{\nu j}) - \kappa^{-l'}j_{l'}(\kappa r_{\nu j})\right) \right]_{r_{\nu j}=S_j} = 0,$$
$$n = 0,1. \quad (31)$$

The principal quantum number required for solving (30) is again fixed by our selection of valence states for the corresponding atom just in the same manner as for the augmented Hankel function discussed above. In passing we note that the radial equations (23) and (30) are identical and, hence, the difference between the augmented functions $\tilde{h}_{l\kappa\sigma}$ and $\tilde{j}_{l\kappa\sigma}$ and the energies $E_{l\kappa i\sigma}^{(H)}$ and $E_{l\kappa i\sigma}^{(J)}$ is only due to the different boundary conditions given by Eqs. (24) and (31). With the augmented Bessel function at hand we arrive at the following expression

for the basis function centered at $\mathbf{R}_{\mu i}$ inside the off-center sphere centered at $\mathbf{R}_{\nu j}$:

$$H^\infty_{L\kappa\sigma}(\mathbf{r}_{\mu i})\Theta_{\nu j} = \sum_{L'} \tilde{J}_{L'\kappa\sigma}(\mathbf{r}_{\nu j}) B_{L'L\kappa}(\mathbf{R}_{\nu j} - \mathbf{R}_{\mu i}). \quad (32)$$

Note that the expansion coefficients in Eqs. (25) and (32) are the same. This is due to the identity of $H_{L\kappa}$ and $\tilde{H}_{L\kappa\sigma}$ as well as $J_{L\kappa}$ and $\tilde{J}_{L\kappa\sigma}$ at the sphere boundary.

Combining finally Eqs. (20), (22), and (32), we construct the full basis function, the augmented spherical wave

$$H^\infty_{L\kappa\sigma}(\mathbf{r}_{\mu i}) = H^i_{L\kappa}(\mathbf{r}_{\mu i}) + \tilde{H}_{L\kappa\sigma}(\mathbf{r}_{\mu i})$$
$$+ \sum_{L'\nu j}(1 - \delta_{\mu\nu}\delta_{ij})\tilde{J}_{L'\kappa\sigma}(\mathbf{r}_{\nu j}) B_{L'L\kappa}(\mathbf{R}_{\nu j} - \mathbf{R}_{\mu i}), \quad (33)$$

which is completely specified by its center, $\mathbf{R}_{\mu i}$, the composite angular momentum index $L = (l, m)$, and the spin index σ. In addition, the augmented spherical wave is continuous and differentiable in all space. Since the ASW basis functions arise from solutions of Schrödinger's equation in the respective portions of space, each of these functions is well adapted to the actual problem and already a relatively small number of basis functions are needed for the expansion of the final wave function. Typically 9 states (s, p, d) per atom are sufficient; for atoms with f electrons we end up with 16 states. This should be contrasted with methods using (augmented) plane waves, where usually hundreds of basis functions per atom are needed.

As concerns the angular momentum indices that accompany each function, we distinguish three sets of partial waves, namely lower, intermediate, and higher waves. While the lower waves enter the secular matrix, the intermediate waves are used only in the expansion in (augmented) Bessel functions. All the remaining partial waves by definition belong to the set of higher waves. In practice, Hankel functions and the low l Bessel functions form the set of lower partial waves, where angular momenta range from 0 to l_{low}. The latter usually is 2 or 3 depending on the atom at hand. The set of intermediate waves comprises all Bessel functions with angular momenta ranging from $l_{\text{low}} + 1$ to l_{int}. Hence, the index L of the Hankel functions in Eq. (33) would run up to $L_{\text{low}} = (l_{\text{low}}, m)$ ant the index L' of the Bessel function would run up to $L_{\text{int}} = (l_{\text{int}}, m)$. As will become obvious later on, it is usually sufficient to set $l_{\text{int}} = l_{\text{low}} + 1$.

In a last step we take into account crystal translational symmetry and use only Bloch sums of basis functions,

$$D^\infty_{L\kappa\sigma}(\mathbf{r}_i, \mathbf{k}) := \sum_\mu e^{i\mathbf{k}\mathbf{R}_\mu} H^\infty_{L\kappa\sigma}(\mathbf{r}_{\mu i}), \quad (34)$$

where

$$\mathbf{r}_i = \mathbf{r} - \tau_i \quad (35)$$

and the symbol D is conventional. Note that we will refer to both functions (33) and (34) as basis functions, but the actual meaning will always be clear from the context.

To prepare for forthcoming sections, we define, in addition, the Bloch sum of the envelope function (20) by

$$D_{L\kappa}(\mathbf{r}_i, \mathbf{k}) := \sum_\mu (1 - \delta_{\mu 0}\delta(\mathbf{r}_i)) e^{i\mathbf{k}\mathbf{R}_\mu} H_{L\kappa}(\mathbf{r}_{\mu i}). \quad (36)$$

Its interstitial part in complete analogy with Eq. (20) then reads as

$$D^i_{L\kappa}(\mathbf{r}_i, \mathbf{k}) := \sum_\mu e^{i\mathbf{k}\mathbf{R}_\mu} H^i_{L\kappa}(\mathbf{r}_{\mu i}) = D_{L\kappa}(\mathbf{r}_i, \mathbf{k})\Theta_I. \quad (37)$$

Moreover, we define the Bloch summed structure constants

$$B_{L'L\kappa}(\tau_j - \tau_i, \mathbf{k})$$
$$:= \sum_\mu (1 - \delta_{\mu\nu}\delta_{ij}) e^{i\mathbf{k}\mathbf{R}_\mu} B_{L'L\kappa}(\tau_j - \tau_i - \mathbf{R}_\mu)$$
$$= 4\pi \sum_{L''} i^{l-l'-l''} \kappa^{l+l'-l''} c_{LL'L''} D_{L''\kappa}(\tau_j - \tau_i, \mathbf{k}), \quad (38)$$

where we have used the identities (27) and (36) in the second step. Hence, for the Bloch summed basis function, we get

$$D^\infty_{L\kappa\sigma}(\mathbf{r}_i, \mathbf{k}) = D^i_{L\kappa}(\mathbf{r}_i, \mathbf{k}) + \tilde{H}_{L\kappa\sigma}(\mathbf{r}_i)$$
$$+ \sum_{L'j} \tilde{J}_{L'\kappa\sigma}(\mathbf{r}_j) B_{L'L\kappa}(\tau_j - \tau_i, \mathbf{k}). \quad (39)$$

The wave function entering the variational procedure may now be written as a linear combination of the just defined Bloch sums,

$$\psi_{\mathbf{k}\sigma}(\mathbf{r}) = \sum_{L\kappa i} c_{L\kappa i\sigma}(\mathbf{k}) D^\infty_{L\kappa\sigma}(\mathbf{r}_i, \mathbf{k}), \quad (40)$$

which is the ASW analogue of the more general equation (1). The coefficients $c_{L\kappa i\sigma}(\mathbf{k})$ arise via the variational principle from the secular equation (6), the explicit construction of which is the subject of the following section.

However, before setting up the secular matrix, we still have to determine the core states. Within the ASW method we are going beyond the so-called frozen core approximation, which uses core states

that arise from a purely atomic calculation without letting them respond to the changes of the valence states, but evaluate the core states from the same radial Schrödinger equation used for the valence states, Eq. (23) or (30), which contain the actual intraatomic potential. Hence the core states feel any changes in the potential due to the valence states and rearrange their shape when the band calculation is iterated to self-consistency. This process is usually referred to as an all electron calculation.

Denoting the radial part of the core states by $\varphi_{\lin_{l_i}}(E_{\lin_{l_i}}, r_{\mu i})$, where n_{l_i} is the principal quantum number, we write down the radial Schrödinger equation

$$\left[-\frac{1}{r_{\mu i}} \frac{\partial^2}{\partial r_{\mu i}^2} r_{\mu i} + \frac{l(l+1)}{r_{\mu i}^2} + v_{i\sigma}^{\mathrm{MT}}(r_{\mu i}) - E_{\lin_{l_i}} \right]$$
$$\times \varphi_{\lin_{l_i}}(E_{\lin_{l_i}}, r_{\mu i}) = 0. \quad (41)$$

The major difference in the valence states is due to the boundary conditions for the core states, which are still subject to the regularity of the radial function at the origin. Yet, in contrast to the valence states, both value and slope at the sphere boundary must vanish since the core states do not take part in the chemical bonding and thus are confined to their respective atomic spheres.

Methods using augmentation for the construction of basis functions offer the special advantage that the valence states by construction are orthogonal to the core states and thus an explicit orthogonalization need not be done. This is due to the fact that the radial parts of the basis functions, i.e., of the augmented Hankel and Bessel functions, obey the same radial Schrödinger equation as the radial parts of the core states. For this reason the radial overlap integral vanishes, as can be easily proven by expressing the integral in terms of the Wronskian of the valence and core radial functions.

The Secular Matrix

While setting up the secular matrix we will, again for simplicity in writing, resort to the so-called scalar–relativistic approximation and omit spin–orbit coupling. Within the local density approximation for the spin-polarized electron gas the Hamiltonian is thus diagonal in spin space,

$$H_\sigma = H_{\sigma\sigma} = -\Delta + v_{\mathrm{eff},\sigma}(\mathbf{r}) \quad (42)$$

with the potential already given in Eq. (13). Defining a bra and ket notation

$$|L\kappa i\rangle^\infty := D_{Lk\sigma}^\infty(\mathbf{r}_i, \mathbf{k}) \quad (43)$$

for the Bloch summed basis functions and using the expansion (40) of the wave function in terms of basis functions, we then arrive at the secular equation

$$\sum_{L'\kappa_2 m} c_{L'\kappa_2 j\sigma}(\mathbf{k}) \big[{}^\infty\langle L\kappa_1 i|H_\sigma|L'\kappa_2 j\rangle_c^\infty$$
$$- E^\infty\langle L\kappa_1 i|L'\kappa_2 j\rangle_c^\infty \big] = 0, \quad (44)$$

where the matrix elements are real space integrals extending over the unit cell. This linear equation system determines the band energies $E = E_\sigma(\mathbf{k})$ as well as the expansion coefficients $c_{Lk_1 i\sigma}(\mathbf{k})$ of the wave function in terms of the basis functions.

To determine the elements of both the Hamiltonian and the overlap matrix we define, in addition, a bra and ket notation for the Bloch summed envelope functions

$$|L\kappa i\rangle := D_{Lk\sigma}(\mathbf{r}_i, \mathbf{k}) \quad (45)$$

and write the general element of the Hamiltonian matrix as

$${}^\infty\langle L\kappa_1 i|H_\sigma|L'\kappa_2 j\rangle_c^\infty$$
$$= \langle L\kappa_1 i|-\Delta|L'\kappa_2 j\rangle_c + \sum_m \big[{}^\infty\langle L\kappa_1 i|H_\sigma|L'\kappa_2 j\rangle_m^\infty$$
$$- \langle L\kappa_1 i|-\Delta|L'\kappa_2 j\rangle_m \big]. \quad (46)$$

Here the index m denotes integration over the atomic sphere centered at τ_m. Furthermore, matrix elements containing $-\Delta$ are to be taken with the nonaugmented envelope functions.

To evaluate the integral (46) we use the fact that in the respective regions of integration the functions entering are eigenfunctions of either the full Hamiltonian H_σ or the free electron Hamiltonian $-\Delta$. The integrals with these operators thus reduce to overlap integrals times the respective eigenenergies, i.e.,

$$\langle L\kappa_1 i|-\Delta|L'\kappa_2 j\rangle_c = \kappa_2^2 \langle L\kappa_1 i|L'\kappa_2 j\rangle_c. \quad (47)$$

Using Eq. (39) for the Bloch summed basis function, we write down the integrals over the atomic spheres with the full Hamiltonian as

$${}^\infty\langle L\kappa_1 i|H_\sigma|L'\kappa_2 j\rangle_m^\infty$$
$$= \delta_{im} E_{lk_2 j\sigma}^{(H)} \langle \tilde{H}_{Lk_1\sigma}|\tilde{H}_{L'\kappa_2\sigma}\rangle_m \delta_{LL'} \delta_{mj}$$
$$+ \delta_{im} E_{l''\kappa_2 m\sigma}^{(J)} \langle \tilde{H}_{Lk_1\sigma}|\tilde{J}_{L''\kappa_2\sigma}\rangle_m \delta_{LL''} B_{L''L'\kappa_2}(\tau_m - \tau_j, \mathbf{k})$$
$$+ B_{L''L\kappa_1}^*(\tau_m - \tau_i, \mathbf{k}) E_{l'\kappa_2 m\sigma}^{(H)} \delta_{L''L'} \langle \tilde{J}_{L''\kappa_1\sigma}|\tilde{H}_{L'\kappa_2\sigma}\rangle_m \delta_{mj}$$
$$+ \sum_{L''} \sum_{L'''} B_{L''L\kappa_1}^*(\tau_m - \tau_i, \mathbf{k}) E_{l'''\kappa_2 m\sigma}^{(J)}$$
$$\times \langle \tilde{J}_{L''\kappa_1\sigma}|\tilde{J}_{L'''\kappa_2\sigma}\rangle_m \delta_{L''L'''} B_{L'''L'\kappa_2}(\tau_m - \tau_j, \mathbf{k})$$

$$= \delta_{im}E^{(H)}_{l\kappa_2 j\sigma}\langle\tilde{H}_{L\kappa_1\sigma}|\tilde{H}_{L\kappa_2\sigma}\rangle_m\delta_{LL'}\delta_{mj}$$

$$+ \delta_{im}E^{(J)}_{l\kappa_2 m\sigma}\langle\tilde{H}_{L\kappa_1\sigma}|\tilde{J}_{L\kappa_2\sigma}\rangle_m B_{LL'\kappa_2}(\tau_m - \tau_j, \mathbf{k})$$

$$+ B^*_{L'L\kappa_1}(\tau_m - \tau_i, \mathbf{k})E^{(H)}_{l'\kappa_2 m\sigma}\langle\tilde{J}_{L'\kappa_1\sigma}|\tilde{H}_{L'\kappa_2\sigma}\rangle_m\delta_{mj}$$

$$+ \sum_{L''} B^*_{L''L\kappa_1}(\tau_m - \tau_i, \mathbf{k})E^{(J)}_{l''\kappa_2 m\sigma}\langle\tilde{J}_{L''\kappa_1\sigma}|\tilde{J}_{L''\kappa_2\sigma}\rangle_m$$

$$\times B_{L''L'\kappa_2}(\tau_m - \tau_j, \mathbf{k}). \tag{48}$$

Here we distinguish three different types of integrals, namely one-, two-, and three-center integrals, depending on the number of sites involved in the integral. One-center integrals contain only augmented Hankel functions, two-center integrals contain both a Hankel and Bessel function, and three-center integrals contain only Bessel functions. Note that the integrals over products of augmented Hankel and/or Bessel functions reduce to radial integrals due to the orthonormality of the spherical harmonics. Whereas those radial integrals, which contain only one type of function for $\kappa_1^2 = \kappa_2^2$, are calculated numerically, the mixed integrals $\langle\tilde{H}_{L\kappa_1\sigma}|\tilde{H}_{L\kappa_2\sigma}\rangle_m$, $\langle\tilde{H}_{L\kappa_1\sigma}|\tilde{J}_{L\kappa_2\sigma}\rangle_m$, and $\langle\tilde{J}_{L\kappa_1\sigma}|\tilde{J}_{L\kappa_2\sigma}\rangle_m$ are expressed in terms of the Hankel and Bessel energies as well as the Wronskians of the respective unaugmented functions taken at the sphere boundary.

While due to the orthonormality of the spherical harmonics, the limitation to the low l Bessel functions is exact in the case of two-center integrals, the three-center integrals still contain an, in principle, infinite summation over L''. However, in the formulation (46) of the general matrix element, three-center integrals enter only in the square bracket term on the right-hand side together with the corresponding integrals built with the envelope functions. Since for high angular momenta the muffin-tin potential in the Hamiltonian H_σ is dominated by the centrifugal term, the augmented functions become identical to the envelope functions and the difference of the two terms in square brackets vanishes. It is thus well justified to omit the difference of three-center terms already for quite low angular momenta. In practice the highest l value used for the three-center integrals, i.e., l_{int}, is set to $l_{\text{low}} + 1$.

The second term in the square bracket on the right-hand side of Eq. (46), i.e., those integrals over the atomic spheres, which contain envelope rather than augmented functions, simply result from Eq. (48) by replacing the Hankel and Bessel energies with κ_2^2 and the augmented functions with

the envelope functions. Hence

$$\langle L\kappa_1 i| - \Delta |L'\kappa_2 j\rangle_m$$

$$= \delta_{im}\kappa_2^2\langle H_{L\kappa_1\sigma}|H_{L\kappa_2\sigma}\rangle_m\delta_{LL'}\delta_{mj}$$

$$+ \delta_{im}\kappa_2^2\langle H_{L\kappa_1\sigma}|J_{L\kappa_2\sigma}\rangle_m B_{LL'\kappa_2}(\tau_m - \tau_j, \mathbf{k})$$

$$+ B^*_{L'L\kappa_1}(\tau_m - \tau_i, \mathbf{k})\kappa_2^2\langle J_{L'\kappa_1\sigma}|H_{L'\kappa_2\sigma}\rangle_m\delta_{mj}$$

$$+ \sum_{L''} B^*_{L''L\kappa_1}(\tau_m - \tau_i, \mathbf{k})\kappa_2^2\langle J_{L''\kappa_1\sigma}|J_{L''\kappa_2\sigma}\rangle_m$$

$$\times B_{L''L'\kappa_2}(\tau_m - \tau_j, \mathbf{k}). \tag{49}$$

The radial integrals appearing in Eq. (49) are calculated using standard identities for the spherical Hankel and Bessel functions: see, e.g., [21, 23].

Next we turn to the first integral in Eq. (46), which extends over the whole unit cell and, according to Eq. (47), can be reduced to the calculation of the corresponding overlap integral. In addition, this term can be combined with the second term in square brackets in Eq. (46). In case both basis functions entering the matrix element are centered at the same site, we end up with just the radial integral $\langle H_{L\kappa_1}|H_{L\kappa_2}\rangle'_j$ extending from the sphere boundary out to infinity. In contrast, if the functions are centered at diﬀerent sites, we can express the overlap integral in terms of structure constants divided by the difference of the κ^2 values or, in case of equal interstitial energies, in terms of the energy derivative of the structure constant. For details of the evaluation, we refer the reader to the original work by Williams, Kübler, and Gelatt as well as to the thesis of the author [21, 23]. We are thus able to write down the general matrix element of the Hamiltonian as

$$^\infty\langle L\kappa_1 i|H_\sigma|L'\kappa_2 j\rangle^\infty_c$$

$$= \left[E^{(H)}_{l\kappa_2 j\sigma}\langle\tilde{H}_{L\kappa_1\sigma}|\tilde{H}_{L\kappa_2\sigma}\rangle_j + \kappa_2^2\langle H_{L\kappa_1}|H_{L\kappa_2}\rangle'_j\right]\delta_{LL'}\delta_{ij}$$

$$+ \frac{\kappa_2^2}{\kappa_2^2 - \kappa_1^2}\left[B_{LL'\kappa_2}(\tau_i - \tau_j, \mathbf{k}) - B^*_{L'L\kappa_1}(\tau_j - \tau_i, \mathbf{k})\right]$$

$$\times \left(1 - \delta(\kappa_1^2 - \kappa_2^2)\right)$$

$$+ \kappa_2^2\dot{B}_{LL'\kappa_1}(\tau_i - \tau_j, \mathbf{k})\delta(\kappa_1^2 - \kappa_2^2)$$

$$+ \left[E^{(J)}_{l\kappa_2 i\sigma}\langle\tilde{H}_{L\kappa_1\sigma}|\tilde{J}_{L\kappa_2\sigma}\rangle_i - \kappa_2^2\langle H_{L\kappa_1}|J_{L\kappa_2}\rangle_i\right]$$

$$\times B_{LL'\kappa_2}(\tau_i - \tau_j, \mathbf{k})$$

$$+ B^*_{L'L\kappa_1}(\tau_j - \tau_i, \mathbf{k})\left[E^{(H)}_{l'\kappa_2 j\sigma}\langle\tilde{J}_{L'\kappa_1\sigma}|\tilde{H}_{L'\kappa_2\sigma}\rangle_j\right.$$

$$\left. - \kappa_2^2\langle J_{L'\kappa_1}|H_{L'\kappa_2}\rangle_j\right]$$

$$+ \sum_m \sum_{L''} B^*_{L''L\kappa_1}(\tau_m - \tau_i, \mathbf{k})$$

$$\times \left[E^{(J)}_{l''\kappa_2 m\sigma} \langle \tilde{J}_{L''\kappa_1\sigma} | \tilde{J}_{L''\kappa_2\sigma} \rangle_m - \kappa_2^2 \langle J_{L''\kappa_1} | J_{L''\kappa_2} \rangle_m \right]$$

$$\times B_{L''L'\kappa_2}(\tau_m - \tau_j, \mathbf{k}). \tag{50}$$

Still we have to calculate the matrix elements of the overlap matrix. They are defined in accordance with Eq. (46) by

$$^\infty \langle L\kappa_1 i | L'\kappa_2 j \rangle^\infty_c = \langle L\kappa_1 i | L'\kappa_2 j \rangle_c$$
$$+ \sum_m \left[{}^\infty \langle L\kappa_1 i | L'\kappa_2 j \rangle^\infty_m - \langle L\kappa_1 i | L'\kappa_2 j \rangle_m \right]. \tag{51}$$

The evaluation of these matrix elements is greatly facilitated by the fact that all the functions entering are eigenfunctions of either the full Hamiltonian H_σ or else free electron Hamiltonian $-\Delta$, which fact, as already mentioned, allows us to reduce the integrals to be built with the partial waves to overlap integrals times the respective eigenvalue. Hence, using the just calculated matrix elements of the Hamiltonian matrix and replacing all energies in Eq. (50) that appear in a numerator with unity, we get for the general matrix element of the overlap matrix

$$^\infty \langle L\kappa_1 i | L'\kappa_2 j \rangle^\infty_c$$
$$= \left[\langle \tilde{H}_{L\kappa_1\sigma} | \tilde{H}_{L\kappa_2\sigma} \rangle_j + \langle H_{L\kappa_1} | H_{L\kappa_2} \rangle'_j \right] \delta_{LL'} \delta_{ij}$$
$$+ \frac{1}{\kappa_2^2 - \kappa_1^2} \left[B_{LL'\kappa_2}(\tau_i - \tau_j, \mathbf{k}) - B^*_{L'L\kappa_1}(\tau_j - \tau_i, \mathbf{k}) \right]$$
$$\times \left(1 - \delta(\kappa_1^2 - \kappa_2^2) \right)$$
$$+ \dot{B}_{LL'\kappa_1}(\tau_i - \tau_j, \mathbf{k}) \delta(\kappa_1^2 - \kappa_2^2)$$
$$+ \left[\langle \tilde{H}_{L\kappa_1\sigma} | \tilde{J}_{L\kappa_2\sigma} \rangle_i - \langle H_{L\kappa_1} | J_{L\kappa_2} \rangle_i \right] B_{LL'\kappa_2}(\tau_i - \tau_j, \mathbf{k})$$
$$+ B^*_{L'L\kappa_1}(\tau_j - \tau_i, \mathbf{k}) \left[\langle \tilde{J}_{L'\kappa_1\sigma} | \tilde{H}_{L'\kappa_2\sigma} \rangle_j - \langle J_{L'\kappa_1} | H_{L'\kappa_2} \rangle_j \right]$$
$$+ \sum_m \sum_{L''} B^*_{L''L\kappa_1}(\tau_m - \tau_i, \mathbf{k})$$
$$\times \left[\langle \tilde{J}_{L''\kappa_1\sigma} | \tilde{J}_{L''\kappa_2\sigma} \rangle_m - \langle J_{L''\kappa_1} | J_{L''\kappa_2} \rangle_m \right]$$
$$\times B_{L''L'\kappa_2}(\tau_m - \tau_j, \mathbf{k}). \tag{52}$$

The present formulation for the elements of the secular matrix offers several advantages: (i) We have separated structural information from intraatomic information by writing each term as a structure constant times intraatomic radial integrals. The latter need to be calculated only once in an iteration before the time-consuming loop over $\mathbf{k}$ points starts. (ii) As can be read off from Eqs. (50) and (52), the intraatomic contributions depend exclusively on integrals over envelope functions, which can be performed analytically: the Hankel and Bessel energies $E^{(H)}_{l\kappa i\sigma}$ and $E^{(J)}_{l\kappa i\sigma}$ and the Hankel and Bessel integrals $S^{(H)}_{l\kappa i\sigma} = \langle \tilde{H}_{L\kappa\sigma} | \tilde{H}_{L\kappa\sigma} \rangle_i$ and $S^{(J)}_{l\kappa i\sigma} = \langle \tilde{J}_{L\kappa\sigma} | \tilde{J}_{L\kappa\sigma} \rangle_i$. Hence, except for the crystal structure information, the secular matrix is completely specified by only four numbers per basis state that contain all information about the shape of the crystal potential. Finally, Eqs. (50) and (52) allow for a very efficient computation, which includes both a high degree of vectorization and low memory costs due to the minimal basis set.

Electronic Charge Density and Magnetization

Because the electronic wave function is an outgrowth of the secular equation at hand, we are able to calculate the electronic charge density as well as the magnetization. They arise as the sum and difference of the spin-dependent charge densities and are made of contributions from both the valence and core electrons. However, since the latter form closed shells, they do not contribute to the magnetization.

Concentrating on the valence electrons first, we write for the charge density

$$\rho_{\mathrm{val}}(\mathbf{r}) = \rho_{\mathrm{val}\uparrow}(\mathbf{r}) + \rho_{\mathrm{val}\downarrow}(\mathbf{r}) \tag{53}$$

and for the magnetization

$$m_{\mathrm{val}}(\mathbf{r}) = \rho_{\mathrm{val}\uparrow}(\mathbf{r}) - \rho_{\mathrm{val}\downarrow}(\mathbf{r}). \tag{54}$$

Within the framework of density functional theory, the spin-dependent charge densities entering Eqs. (53) and (54) are given by

$$\rho_{\mathrm{val},\sigma}(\mathbf{r}) = \sum_\mathbf{k} |\psi_{\mathbf{k}\sigma}(\mathbf{r})|^2 \Theta(E_F - E_\sigma(\mathbf{k})). \tag{55}$$

Here we have implied the use of Fermi statistics by summing over the occupied states up to the Fermi energy E_F. The wave function is that defined by Eq. (40) with the coefficients determined by the solution of the eigenproblem (44).

Following the notions of density functional theory, we have to combine Eqs. (55) and (40) with the expression (39) for the ASW basis function and calculate the spin-dependent charge density. However, within the standard ASW method there exists an alternative procedure: First recall that we started out from a muffin-tin potential. For this reason, the potential to be extracted later on from the charge density likewise must be a muffin-tin potential since density functional theory poses a self-consistent field problem. Hence we may already reduce the charge density to its muffin-tin form. Within this so-called shape approximation, we thus concentrate on the spherical symmetric spin-dependent charge density within the atomic spheres. In addition, we

strictly enforce the ASA, i.e., we ignore the interstitial region completely and treat the atomic spheres as nonoverlapping. However, the spherical symmetric charge density may likewise be extracted from the electronic density of states, which offers the additional advantage of an increased accuracy since within the Rayleigh–Ritz variational procedure, the eigenenergies are determined to a higher accuracy than the eigenfunctions [19, 21, 47].

To start with, we write down the charge density in the form it would have in the more accurate KKR method [22, 42, 43]:

$$\rho_{\mathrm{val},i\sigma}(r_i) = \frac{1}{4\pi} \int_{-\infty}^{E_F} dE \sum_l \rho_{li\sigma}(E) R_{l\sigma}^2(E, r_i). \quad (56)$$

The functions $R_{l\sigma}(E, r_i)$ are normalized regular solutions of the radial Schrödinger equation (23) to energy E, and $\rho_{li\sigma}(E)$ denotes the density of states decomposed according to angular momentum, atomic site, and spin.

Within the ASW method, an equivalent analysis of the total density of states can be achieved by decomposing the norm of the wave function, which follows directly from the expansion (40) of the wave functions in terms of the basis functions

$$\int_{\Omega_c} d^3\mathbf{r} \left| \psi_{\mathbf{k}\sigma}(\mathbf{r}) \right|^2 = \sum_{L\kappa_1 i} \sum_{L'\kappa_2 j} c_{L\kappa_1 i\sigma}^*(\mathbf{k}) c_{L'\kappa_2 j\sigma}(\mathbf{k})$$
$$\times {}^\infty\langle L\kappa_1 i | L'\kappa_2 j \rangle_c^\infty. \quad (57)$$

Inserting the expression (52) for the overlap integral and using the definition

$$a_{L\kappa i\sigma}(\mathbf{k}) = \sum_{L'j} c_{L'\kappa j\sigma}(\mathbf{k}) B_{LL'\kappa}(\tau_i - \tau_j, \mathbf{k}), \quad (58)$$

we get

$$\int_{\Omega_c} d^3\mathbf{r} \left| \psi_{\mathbf{k}\sigma}(\mathbf{r}) \right|^2$$
$$= \sum_{L\kappa_1\kappa_2 i} \Big[c_{L\kappa_1 i\sigma}^*(\mathbf{k}) c_{L\kappa_2 i\sigma}(\mathbf{k}) \big[\langle \tilde{H}_{L\kappa_1\sigma} | \tilde{H}_{L\kappa_2\sigma} \rangle_i$$
$$+ \langle H_{L\kappa_1} | H_{L\kappa_2} \rangle_i' \big]$$
$$+ c_{L\kappa_1 i\sigma}^*(\mathbf{k}) \sum_{L'j} c_{L'\kappa_2 j\sigma}(\mathbf{k}) \frac{1}{\kappa_2^2 - \kappa_1^2}$$
$$\times \big[B_{LL'\kappa_2}(\tau_i - \tau_j, \mathbf{k}) - B_{L'L\kappa_1}^*(\tau_j - \tau_i, \mathbf{k}) \big]$$
$$\times \big(1 - \delta(\kappa_1^2 - \kappa_2^2) \big)$$
$$+ c_{L\kappa_1 i\sigma}^*(\mathbf{k}) \sum_{L'j} c_{L'\kappa_2 j\sigma}(\mathbf{k}) \dot{B}_{LL'\kappa_1}(\tau_i - \tau_j, \mathbf{k})$$
$$\times \delta(\kappa_1^2 - \kappa_2^2)$$
$$+ c_{L\kappa_1 i\sigma}^*(\mathbf{k}) a_{L\kappa_2 i\sigma}(\mathbf{k}) \big[\langle \tilde{H}_{L\kappa_1\sigma} | \tilde{J}_{L\kappa_2\sigma} \rangle_i - \langle H_{L\kappa_1} | J_{L\kappa_2} \rangle_i \big]$$

$$+ a_{L\kappa_1 i\sigma}^*(\mathbf{k}) c_{L\kappa_2 i\sigma}(\mathbf{k}) \big[\langle \tilde{J}_{L\kappa_1\sigma} | \tilde{H}_{L\kappa_2\sigma} \rangle_i - \langle J_{L\kappa_1} | H_{L\kappa_2} \rangle_i \big]$$
$$+ a_{L\kappa_1 i\sigma}^*(\mathbf{k}) a_{L\kappa_2 i\sigma}(\mathbf{k}) \big[\langle \tilde{J}_{L\kappa_1\sigma} | \tilde{J}_{L\kappa_2\sigma} \rangle_i - \langle J_{L\kappa_1} | J_{L\kappa_2} \rangle_i \big] \Big]. \quad (59)$$

As already mentioned in the previous sections, Hankel and Bessel functions are included up to l_{low} and l_{int}, respectively. Equation (59) is the exact representation of the norm, which, however, does not allow for a decomposition into partial densities of states due to the double sum in the second and third term on the right-hand side. These terms originate from the so-called "combined correction," i.e., from the difference of the first term and the third term (in square brackets) on the right-hand side of Eq. (46). Since we already opted for the ASA in the present context, these terms cancel out from the norm and we write down instead the norm as calculated with the ASA:

$$\int_{\Omega_c} d^3\mathbf{r} \left| \psi_{\mathbf{k}\sigma}(\mathbf{r}) \right|^2$$
$$= \sum_{L\kappa_1\kappa_2 i} \Big[c_{L\kappa_1 i\sigma}^*(\mathbf{k}) c_{L\kappa_2 i\sigma}(\mathbf{k}) \langle \tilde{H}_{L\kappa_1\sigma} | \tilde{H}_{L\kappa_2\sigma} \rangle_i$$
$$+ c_{L\kappa_1 i\sigma}^*(\mathbf{k}) a_{L\kappa_2 i\sigma}(\mathbf{k}) \langle \tilde{H}_{L\kappa_1\sigma} | \tilde{J}_{L\kappa_2\sigma} \rangle_i$$
$$+ a_{L\kappa_1 i\sigma}^*(\mathbf{k}) c_{L\kappa_2 i\sigma}(\mathbf{k}) \langle \tilde{J}_{L\kappa_1\sigma} | \tilde{H}_{L\kappa_2\sigma} \rangle_i$$
$$+ a_{L\kappa_1 i\sigma}^*(\mathbf{k}) a_{L\kappa_2 i\sigma}(\mathbf{k}) \langle \tilde{J}_{L\kappa_1\sigma} | \tilde{J}_{L\kappa_2\sigma} \rangle_i \Big] + \Delta_\sigma(\mathbf{k})$$
$$=: \sum_{li} q_{li\sigma}(\mathbf{k})$$
$$\overset{!}{=} 1. \quad (60)$$

Here we have added a quantity $\Delta_\sigma(\mathbf{k})$, which accounts for the exactly known but small difference between the expressions (59) and (60). However, since this quantity makes only a small contribution to the norm, it is omitted in practice and the resulting deviation of the norm from unity is cured by a renormalization of the remaining terms. As indicated in the second to last line of Eq. (60), we thus arrive at the desired unique decomposition of the norm, which allows us to calculate partial densities of states,

$$\rho_{li\sigma}(E) := \sum_{\mathbf{k}} \delta(E - E_\sigma(\mathbf{k})) q_{li\sigma}(\mathbf{k}). \quad (61)$$

Still, the linear methods offer another advantage for calculating the electronic densities of states in terms of its moments, which are defined by

$$M_{li\sigma}^{(k)} = \int_{-\infty}^{E_F} dE\, E^k \rho_{li\sigma}(E), \qquad k = 0, 1, 2. \quad (62)$$

If the energy dependence of the radial wave function were perfectly linear, the partial density of states would be completely specified by its first three moments. Yet, deviations from the linear behavior do exist, but since they are small, it suffices to include, in addition, the fourth moment. We are then able to define a new density of states

$$\bar{\rho}_{li\sigma}(E) := \sum_{\alpha=1}^{2} \delta\big(E - E_{li\sigma}^{(\alpha)}\big)Q_{li\sigma}^{(\alpha)}, \quad (63)$$

where the two energies $E_{li\sigma}^{(\alpha)}$ and the charges $Q_{li\sigma}^{(\alpha)}$ are subject to the condition that they yield the same first four moments as the true charge density does,

$$\sum_{\alpha=1}^{2} \big(E_{li\sigma}^{(\alpha)}\big)^k Q_{li\sigma}^{(\alpha)} \stackrel{!}{=} \int_{-\infty}^{E_F} dE\, E^k \rho_{li\sigma}(E),$$

$$k = 0,1,2,3. \quad (64)$$

With the true density of states replaced by the expression (63), we arrive at the representation of the spin-dependent charge density,

$$\rho_{\mathrm{val},i\sigma}(r_i) = \frac{1}{4\pi} \sum_{l} \sum_{\alpha=1}^{2} Q_{li\sigma}^{(\alpha)} R_{l\sigma}^2\big(E_{li\sigma}^{(\alpha)}, r_i\big)$$

$$= \sum_{l} \rho_{\mathrm{val},li\sigma}(r_i), \quad (65)$$

which does not require the full energy dependence of the radial Schrödinger equation solution, but only solutions at two different energies.

The previous results reveal an additional "symmetry" of the standard ASW method. Obviously, the intraatomic charge density is completely specified by only two energies $E_{li\sigma}^{(\alpha)}$ and charges $Q_{li\sigma}^{(\alpha)}$. This should likewise be related to the four quantities per orbital that entered the secular matrix, namely the Hankel and Bessel energies and integrals. The whole iteration process can thus be cut into two parts. The band calculation starts from the Hankel and Bessel energies and integrals, and returns the above energies $E_{li\sigma}^{(\alpha)}$ and charges $Q_{li\sigma}^{(\alpha)}$. In case of the intraatomic calculation, things are reversed. This finally allows for an additional speed up of the method, which will be outlined in more detail in the following section.

Finally, we complement the valence charge density with the core charge density, which is given by

$$\rho_{\mathrm{core}}(\mathbf{r}) = \sum_{i} \rho_{\mathrm{core}}(r_i)$$

$$= \sum_{in_{l_i}lm} \varphi_{lin_{l_i}}^2\big(E_{lin_{l_i}}, r_i\big)\big|Y_L(\hat{\mathbf{r}}_i)\big|^2$$

$$= \sum_{in_{l_i}l} \frac{2l+1}{4\pi}\varphi_{lin_{l_i}}^2\big(E_{lin_{l_i}}, r_i\big)$$

$$= \sum_{i} \rho_{\mathrm{core}}(r_i), \quad (66)$$

with the core state wave functions $\varphi_{lin_{l_i}}(E_{lin_{l_i}}, r_i)$ and energies $E_{lin_{l_i}}$ arising from the radial Schrödinger equation (41) subject to the conditions of vanishing value and slope at the sphere boundary.

The Effective Potential

To close the self-consistency cycle, we still have to calculate the effective potential as seen by the electrons. Within density functional theory and the local density approximation, which in an approximate manner cast the full many body problem into a single-particle self-consistent field problem, the potential arises as the sum of the external, Hartree, and exchange–correlation potentials [4, 5, 7, 22, 61]. While the external potential is just the Coulomb potential originating from the nuclei and possibly external electromagnetic fields, the Hartree potential embodies the classical contribution to the electron–electron Coulomb interaction, the nonclassical parts of which are contained in the exchange–correlation potential.

For practical calculations it is useful to combine the charge density of the electrons as calculated in the previous section with the charge density of the nuclei:

$$\rho_{\mathrm{nucl}}(\mathbf{r}) = -\sum_{i} \delta(\mathbf{r}_i)Z_i. \quad (67)$$

The classical potential due to the resulting total charge density then contains both the external and the Hartree potential. It can be written as

$$v_{cc}(\mathbf{r}) = 2\int d^3\mathbf{r}' \frac{\rho_{\mathrm{el}}(\mathbf{r}')}{|\mathbf{r}-\mathbf{r}'|} - 2\sum_{\mu i}\frac{Z_i}{|\mathbf{r}-\mathbf{R}_{\mu i}|}$$

$$= 2\sum_{\mu i}\int_{\Omega_i} d^3\mathbf{r}'_{\mu i}\frac{\rho_{\mathrm{el}}(\mathbf{r}'_{\mu i})}{|\mathbf{r}_{\mu i}-\mathbf{r}'_{\mu i}|} - 2\sum_{\mu i}\frac{Z_i}{|\mathbf{r}_{\mu i}|}, \quad (68)$$

where the prefactor 2 is due to our choice of atomic units. Next we assume the position $\mathbf{r}$ to lie in the atomic sphere centered at site $\mathbf{R}_{\nu j}$. Using the identity [62]

$$\frac{1}{|\mathbf{r}-\mathbf{r}'|} = \sum_{L}\frac{4}{2l+1}\frac{r_<^l}{r_>^{l+1}}Y_L^*(\hat{\mathbf{r}})Y_L(\hat{\mathbf{r}}'), \quad (69)$$

we transform Eq. (68) to the expression

$$
\begin{aligned}
v_{\mathrm{cc}}(\mathbf{r})|_{|\mathbf{r}_{vj}| \leq S_j} = {} & 8\pi \frac{1}{r_{vj}} \int_0^{r_{vj}} dr'_{vj}\, r'^2_{vj} \rho_{\mathrm{el}}(r'_{vj}) \\
& + 8\pi \int_{r_{vj}}^{S_i} dr'_{vj}\, r'_{vj} \rho_{\mathrm{el}}(r'_{vj}) - 2\frac{Z_i}{|\mathbf{r}_{vj}|} \\
& + 2\sum_{\mu i}(1 - \delta_{\mu v}\delta_{ij})\frac{Q_i - Z_i}{|\mathbf{r}_{\mu i}|}, \qquad (70)
\end{aligned}
$$

which is based on the shape approximation chosen in the previous section, i.e., on the assumption of spherical symmetric charge densities confined to atomic spheres. With the shape approximation in mind, we may furthermore treat all the charges within the atomic spheres as point charges,

$$
Q_i = 4\pi \int_0^{S_i} dr'_{\mu i}\, r'^2_{\mu i} \rho_{\mathrm{el}}(r'_{\mu i}). \qquad (71)
$$

As well known a spherical symmetric charge density within a sphere acts like a point charge at the center of the sphere. Taken together with the nuclear charges, these "electronic point charges" generate the Madelung potential, which is represented by the last term in Eq. (70). Actually this treatment is not fully correct because it neglects the overlap of atomic spheres. In the atomic sphere approximation there is a finite overlap of the atomic spheres, which leads to errors when the interatomic interactions between electronic charges are treated in the way just described. Obviously this error is smaller in closed packed solids since there the overlap can be minimized [63, 64]. For open structures it has become standard practice to insert so-called empty spheres into the unit cell, which, together with the physical spheres, enable an artificial close packing and, hence, allow the sphere overlap to be minimized. Nevertheless, in practice it remains a challenge to find (i) optimal empty sphere positions and (ii) optimal radii for all spheres. To achieve an efficient solution of the aforementioned problem, we recently devised the sphere geometry optimization (SGO) algorithm [27], which is capable of handling even complicated crystal structures and has proven to be very fast. In short, the SGO method is based on the observation that the full crystal potential is well approximated by the overlapping free atom potential of the constituent atoms [65] and thus could be used for the selection of empty sphere positions and sphere radii *before* the self-consistent calculation is actually started [66].

Still we can substantially simplify the Madelung term in Eq. (70) by enforcing the muffin-tin shape of the potential again. Due to the spherical sym-

metry of the potential within the atomic spheres, which suppresses the angular degrees of freedom, the Madelung potential, e.g., in the sphere at site $\mathbf{R}_{vj}$ can in no way depend on the position $\mathbf{r}_{vj}$ within that sphere. For that reason the Madelung potential reduces to

$$
v_{\mathrm{Mad},j} = 2\sum_{\mu i}(1 - \delta_{0\mu}\delta_{ij})\frac{Q_i - Z_i}{|\boldsymbol{\tau}_j - \boldsymbol{\tau}_i - \mathbf{R}_\mu|}, \qquad (72)
$$

which is just a constant shift of the energy scale within each atomic sphere. Using the identity

$$
H_{L\kappa}(\boldsymbol{\tau}_j - \boldsymbol{\tau}_i - \mathbf{R}_\mu)|_{l=0,\,\kappa\to 0} = \frac{1}{\sqrt{4\pi}}\frac{1}{|\boldsymbol{\tau}_j - \boldsymbol{\tau}_i - \mathbf{R}_\mu|}, \qquad (73)
$$

we can express the lattice sum in Eq. (72) in terms of the Bloch summed Hankel functions (36) for $\mathbf{k} = 0$ and get for the Madelung potential

$$
\begin{aligned}
v_{\mathrm{Mad},j} = {} & 2\sum_{\mu i}(1 - \delta_{0\mu}\delta_{ij})\sqrt{4\pi}\, H_{L\kappa}(\boldsymbol{\tau}_j - \boldsymbol{\tau}_i - \mathbf{R}_\mu) \\
& \times (Q_i - Z_i)|_{l=0,\,\kappa\to 0} \\
= {} & 2\sum_i \sqrt{4\pi}\, D_{L\kappa}(\boldsymbol{\tau}_j - \boldsymbol{\tau}_i, 0)(Q_i - Z_i)|_{l=0,\,\kappa\to 0}.
\end{aligned} \qquad (74)
$$

Note that those parts of the Bloch summed Hankel function $D_{L\kappa}$ that do not depend on the vector $\boldsymbol{\tau}_j - \boldsymbol{\tau}_i$ cancel out due to charge neutrality of the unit cell,

$$
\sum_i (Q_i - Z_i) \overset{!}{=} 0. \qquad (75)
$$

Next we evaluate the exchange–correlation potential as supplied by the local density approximation, which is a spin-dependent local function of the spin-dependent electronic charge densities [5–8, 22, 61]. We thus write

$$
\begin{aligned}
v_{\mathrm{xc},\sigma}(\mathbf{r}) &= v_{\mathrm{xc},\sigma}\big[\rho_{\mathrm{el},\sigma}(\mathbf{r}), \rho_{\mathrm{el},-\sigma}(\mathbf{r})\big] \\
&= \sum_i v_{\mathrm{xc},i\sigma}\big[\rho_{\mathrm{el},\sigma}(\mathbf{r}_i), \rho_{\mathrm{el},-\sigma}(\mathbf{r}_i)\big] \\
&= \sum_i v_{\mathrm{xc},i\sigma}(\mathbf{r}_i). \qquad (76)
\end{aligned}
$$

The actual parametrization of the exchange–correlation potential is taken from Hedin and Lundqvist, von Barth and Hedin as well as Moruzzi, Janak, and Williams [22, 67–69].

Finally, combining Eqs. (70), (74), and (76), we arrive at the result for the effective single-particle potential,

$$
v_\sigma(\mathbf{r}) = v_{\mathrm{cc}}(\mathbf{r}) + v_{\mathrm{xc},\sigma}(\mathbf{r})
$$

$$= \sum_i \left[v_{cc,i}(\mathbf{r}_i) + v_{xc,i\sigma}(\mathbf{r}_i) + v_{Mad,i} \right]$$

$$= \sum_i v_\sigma(\mathbf{r}_i), \tag{77}$$

where

$$v_{cc,i}(\mathbf{r}_i) = 8\pi \frac{1}{r_i} \int_0^{r_i} dr_i' \, r_i'^2 \rho_{el}(r_i')$$

$$+ 8\pi \int_{r_i}^{S_i} dr_i' \, r_i' \rho_{el}(r_i') - 2\frac{Z_i}{|\mathbf{r}_i|}. \tag{78}$$

Hence, in the same manner as the charge density, the potential is made of intraatomic contributions from all spheres.

Actually, we have closed the self-consistency cycle at this point, since the just derived potential can be inserted into Schrödinger's equations (23) and (30), which allows for the calculation of new augmented Hankel and Bessel functions. Nevertheless, there is an additional bonus of the ASW method due to the previous separation of the Madelung potential, which causes only a constant shift within each atomic sphere and, hence, leads to an effective decoupling of all the intraatomic problems. We are thus able to calculate the intraatomic potential according to Eq. (77) without taking the Madelung term into account. After this step, instead of feeding the potential directly into the following band calculation, we may again insert it into the Schrödinger equation to calculate new radial functions and a new charge density, and thereby establish an intraatomic self-consistency cycle. This allows for a potential that is self-consistently calculated within each atom before all these atomic potentials are combined for the following step of the band iteration.

To be specific, following the flow diagram given in Figure 1, we start from the energies $E_{li\sigma}^{(\alpha)}$ and charges $Q_{li\sigma}^{(\alpha)}$ resulting from the momentum analysis of the partial densities of states. The energies are then transformed to the local energy scale by

$$\bar{E}_{li\sigma}^{(\alpha)} = E_{li\sigma}^{(\alpha)} - v_{Mad,i}. \tag{79}$$

After this we solve the radial Schrödinger equation

$$\left[-\frac{1}{r_i}\frac{\partial^2}{\partial r_i^2} r_i + \frac{l(l+1)}{r_i^2} + v_{cc,i}(\mathbf{r}_i) + v_{xc,i\sigma}(\mathbf{r}_i) - \bar{E}_{li\sigma}^{(\alpha)} \right]$$

$$\times R_{l\sigma}\left(\bar{E}_{li\sigma}^{(\alpha)}, r_i\right) = 0, \tag{80}$$

where $R_{l\sigma}(\bar{E}_{li\sigma}^{(\alpha)}, r_i)$ is a real and regular function normalized to

$$\int_0^{S_i} dr_i \, r_i^2 \left| R_{l\sigma}\left(\bar{E}_{li\sigma}^{(\alpha)}, r_i\right) \right|^2 = Q_{li\sigma}^{(\alpha)}. \tag{81}$$
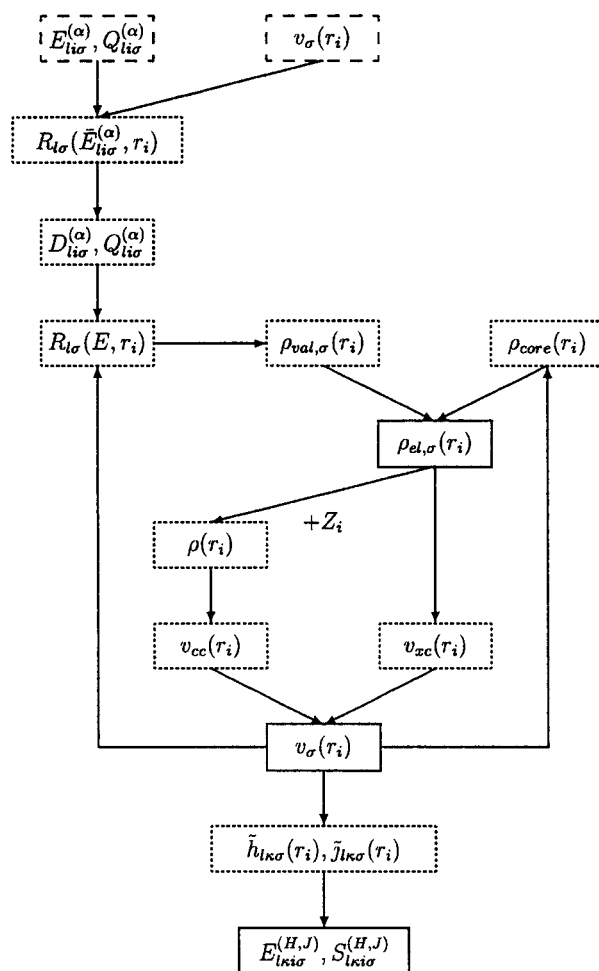
FIGURE 1. Flow diagram of the intraatomic calculations of the standard ASW method. Input and output variables are highlighted by dashed and solid boxes, respectively.

Next, from the solution of the radial equation (80), we take the logarithmic derivatives at the sphere boundary,

$$D_{li\sigma}^{(\alpha)} = r_i \left[R_{l\sigma}\left(\bar{E}_{li\sigma}^{(\alpha)}, r_i\right) \right]^{-1} \frac{\partial}{\partial r_i} R_{l\sigma}\left(\bar{E}_{li\sigma}^{(\alpha)}, r_i\right)\Big|_{r_i = S_i}, \tag{82}$$

and thus arrive at a set of four new quantities per basis state, namely the logarithmic derivatives $D_{li\sigma}^{(\alpha)}$ and the charges $Q_{li\sigma}^{(\alpha)}$. As experience has shown, the logarithmic derivatives are superior to the energies $E_{li\sigma}^{(\alpha)}$ since they allow for a more stable acceleration of the iteration process toward self-consistency. In the course of this acceleration process, the logarithmic derivatives and the charges of the actual iteration as well as previous ones are used to make a good choice for use in the following iteration. There exist

several methods to accelerate the iteration processes in electronic structure calculations, which have been reviewed recently [26]. In addition to this more numerical advantage of the logarithmic derivatives, they allow for a better illustration of the aforementioned interplay between intraatomic and band calculations. This has been used already in the concept of "renormalized atoms," which corresponds to atomic calculations subject to boundary conditions that reflect the influence of the surrounding atoms [21, 53–55]. It is this concept, which, according to Williams, Kübler, and Gelatt, influenced the development of the ASW method to a large degree [21].

With the logarithmic derivatives at hand we may finally enter the intraatomic iteration cycle as sketched in Figure 1. After self-consistency has been achieved, the muffin-tin potential is used in a last step with the radial Schrödinger equations (23) and (30) to evaluate the Hankel and Bessel energies $E_{lki\sigma}^{(H)}$ and $E_{lki\sigma}^{(J)}$ as well as the Hankel and Bessel integrals $S_{lki\sigma}^{(H)}$ and $S_{lki\sigma}^{(J)}$. The latter quantities then enter the subsequent band calculation.

The Total Energy

Although it is outside the self-consistency cycle, the total energy gives important information about binding properties, bulk moduli, elastic constants or the stability of different magnetic structures. It is usually written as a sum over all single-particle core and valence state energies minus the so-called double counting terms [7, 22, 61]. Adding the contribution arising from the energy due to the Coulomb interaction of the nuclei with each other, which is not covered by density functional theory, we write

$$
\begin{aligned}
E_T &= E\big[\rho_{\text{el},\sigma}(\mathbf{r}), \rho_{\text{el},-\sigma}(\mathbf{r})\big] \\
&= \sum_{\mathbf{k}\sigma} E_\sigma(\mathbf{k})\Theta\big(E_F - E_\sigma(\mathbf{k})\big) + \sum_{in_{l_i}lm\sigma} E_{lin_{l_i}} \\
&\quad - \frac{1}{N}\int\int d^3\mathbf{r}\, d^3\mathbf{r}'\, \frac{\rho_{\text{el}}(\mathbf{r})\rho_{\text{el}}(\mathbf{r}')}{|\mathbf{r}-\mathbf{r}'|} \\
&\quad - \frac{1}{N}\sum_\sigma \int d^3\mathbf{r}\, v_{\text{xc},\sigma}(\mathbf{r})\rho_{\text{el},\sigma}(\mathbf{r}) \\
&\quad + \sum_\sigma E_{\text{xc},\sigma}\big[\rho_{\text{el},\sigma}(\mathbf{r}), \rho_{\text{el},-\sigma}(\mathbf{r})\big] \\
&\quad + \frac{1}{N}\sum_{\mu\nu}\sum_{ij}(1 - \delta_{\mu\nu}\delta_{ij})\frac{Z_i Z_j}{|\mathbf{R}_{\nu j} - \mathbf{R}_{\mu i}|}. \quad (83)
\end{aligned}
$$

Here all integrations extend over the whole crystal. As for the construction of the exchange–correlation

potential in the preceding section, we use the local density approximation for the exchange–correlation energy functional [22]

$$
\begin{aligned}
&E_{\text{xc},\sigma}\big[\rho_{\text{el},\sigma}(\mathbf{r}), \rho_{\text{el},-\sigma}(\mathbf{r})\big] \\
&\quad = \frac{1}{N}\int d^3\mathbf{r}\, \varepsilon_{\text{xc},\sigma}\big[\rho_{\text{el},\sigma}(\mathbf{r}), \rho_{\text{el},-\sigma}(\mathbf{r})\big]\rho_{\text{el},\sigma}(\mathbf{r}). \quad (84)
\end{aligned}
$$

According to this approximation, the function $\varepsilon_{\text{xc},\sigma}$ is a local function of the spin-dependent charge densities. In complete analogy to Eq. (76), we thus note

$$
\begin{aligned}
\varepsilon_{\text{xc},\sigma}(\mathbf{r}) &= \varepsilon_{\text{xc},\sigma}\big[\rho_{\text{el},\sigma}(\mathbf{r}), \rho_{\text{el},-\sigma}(\mathbf{r})\big] \\
&= \sum_i \varepsilon_{\text{xc},i\sigma}\big[\rho_{\text{el},\sigma}(\mathbf{r}_i), \rho_{\text{el},-\sigma}(\mathbf{r}_i)\big] \\
&= \sum_i \varepsilon_{\text{xc},i\sigma}(\mathbf{r}_i). \quad (85)
\end{aligned}
$$

Again we use the explicit parametrization given by Hedin and Lundqvist, von Barth and Hedin as well as Moruzzi, Janak, and Williams [22, 67–69].

As for the effective single-particle potential, we will derive in the following a formulation of the total energy that allows for a simple evaluation and interpretation of the results in terms of atomic contributions and a Madelung energy,

$$
E_T = \sum_i E_{T,i} + E_{\text{Mad}}. \quad (86)
$$

The band energy contribution to the total energy, which is the first term on the right-hand side of Eq. (83), may be simplified with the help of definition (61) of the partial densities of states as well as the alternative representation (63) arising from the momentum analysis. We thus note

$$
\begin{aligned}
&\sum_{\mathbf{k}\sigma} E_\sigma(\mathbf{k})\Theta\big(E_F - E_\sigma(\mathbf{k})\big) \\
&\quad = \sum_\sigma \int_{-\infty}^{E_F} dE \sum_{\mathbf{k}} E_\sigma(\mathbf{k})\delta\big(E - E_\sigma(\mathbf{k})\big) \\
&\quad = \sum_{li\sigma} \int_{-\infty}^{E_F} dE\, E\rho_{li\sigma}(E) \\
&\quad = \sum_{li\sigma}\sum_{\alpha=1}^{2} E_{li\sigma}^{(\alpha)}Q_{li\sigma}^{(\alpha)}. \quad (87)
\end{aligned}
$$

With the help of Eq. (79) we can still split off the local Madelung potential. Defining an analogous energy shift for the core states by

$$
\bar{E}_{lin_{l_i}} := E_{lin_{l_i}} - v_{\text{Mad},i}, \quad (88)
$$

we get

$$
\sum_{\mathbf{k}\sigma} E_\sigma(\mathbf{k})\Theta\big(E_F - E_\sigma(\mathbf{k})\big) + \sum_{in_{l_i}lm\sigma} E_{lin_{l_i}}
$$

$$= \sum_{li\sigma}\left[\sum_{\alpha=1}^{2}\bar{E}_{li\sigma}^{(\alpha)}Q_{li\sigma}^{(\alpha)} + (2l+1)\sum_{n_{l_i}}\bar{E}_{lin_{l_i}}\right]$$
$$+ \sum_i v_{\mathrm{Mad},i}\left[\sum_{l\sigma}\sum_{\alpha=1}^{2}Q_{li\sigma}^{(\alpha)} + 2\sum_{n_{l_i}l}(2l+1)\right],$$

(89)

where the last term in square brackets on the right-hand side is the total electronic charge inside the atomic sphere at site $\boldsymbol{\tau}_i$, which was defined as Q_i in Eq. (71). From Eqs. (65) and (66), we have, in addition,

$$\sum_{l\sigma}\sum_{\alpha=1}^{2}Q_{li\sigma}^{(\alpha)} = 4\pi\sum_\sigma\int_0^{S_i}\rho_{\mathrm{val},i\sigma}(r_i)$$

(90)

and

$$2\sum_{n_i l}(2l+1) = 4\pi\sum_\sigma\int_0^{S_i}\rho_{\mathrm{core},i}(r_i).$$

(91)

Combining now Eqs. (89)–(91) we arrive at the following expression for the sum of the single-particle energies:

$$\sum_{\mathbf{k}\sigma}E_\sigma(\mathbf{k})\Theta\big(E_F - E_\sigma(\mathbf{k})\big) + \sum_{in_i lm\sigma}E_{lin_i}$$
$$= \sum_{li\sigma}\left[\sum_{\alpha=1}^{2}\bar{E}_{li\sigma}^{(\alpha)}Q_{li\sigma}^{(\alpha)} + (2l+1)\sum_{n_i}\bar{E}_{lin_i}\right]$$
$$+ \sum_i v_{\mathrm{Mad},i}Q_i.$$

(92)

Next we turn to the third term on the right-hand side of Eq. (83), which is the so-called double counting term. As a consequence of our previous option for the ASA and the neglect of the interstitial region of the crystal, the integrals appearing in the double counting term can be decomposed into a sum of integrals over the atomic spheres. In the same manner as for the construction of the Hartree potential, the latter integrals may be replaced by point charges located at the sphere centers whenever the twofold integral runs over different spheres. We thus note

$$\frac{1}{N}\int\int d^3\mathbf{r}\,d^3\mathbf{r}'\frac{\rho_{\mathrm{el}}(\mathbf{r})\rho_{\mathrm{el}}(\mathbf{r}')}{|\mathbf{r} - \mathbf{r}'|}$$
$$= \frac{1}{N}\sum_{\mu\nu}\sum_{ij}\int_{\Omega_i}\int_{\Omega_j}d^3\mathbf{r}_{\mu i}\,d^3\mathbf{r}'_{\nu j}\frac{\rho_{\mathrm{el},i}(\mathbf{r}_i)\rho_{\mathrm{el},j}(\mathbf{r}'_j)}{|\mathbf{r}_{\mu i} - \mathbf{r}'_{\nu j}|}$$
$$= \sum_i\int_{\Omega_i}\int_{\Omega_i}d^3\mathbf{r}_i\,d^3\mathbf{r}'_i\frac{\rho_{\mathrm{el},i}(\mathbf{r}_i)\rho_{\mathrm{el},i}(\mathbf{r}'_i)}{|\mathbf{r}_i - \mathbf{r}'_i|}$$
$$+ \frac{1}{N}\sum_{\mu\nu}\sum_{ij}(1 - \delta_{\mu\nu}\delta_{ij})\frac{Q_iQ_j}{|\mathbf{R}_{\mu i} - \mathbf{R}_{\nu j}|}.$$

(93)

Again we point out that strictly speaking this treatment is erroneous since the atomic spheres *do* overlap.

Still we have to check the fourth and fifth terms on the right-hand side of Eq. (83), which correspond to the exchange–correlation energy. Since in the local density approximation the integrals appearing in these terms likewise decompose into a sum of integrals over atomic spheres, we get

$$E_{\mathrm{xc},\sigma}\big[\rho_{\mathrm{el},\sigma}(\mathbf{r}), \rho_{\mathrm{el},-\sigma}(\mathbf{r})\big] - \frac{1}{N}\int d^3\mathbf{r}\,v_{\mathrm{xc},\sigma}(\mathbf{r})\rho_{\mathrm{el},\sigma}(\mathbf{r})$$
$$= \sum_i\int_{\Omega_i}d^3\mathbf{r}_i\big[\varepsilon_{\mathrm{xc},i\sigma}(\mathbf{r}_i) - v_{\mathrm{xc},i\sigma}(\mathbf{r}_i)\big]\rho_{\mathrm{el},i\sigma}(\mathbf{r}_i). \quad (94)$$

Comparing now Eqs. (92)–(94) to the original expression (83) as well as the definition (72) of the Madelung potential, we have arrived at a formulation of the total energy that consists of a single sum over atoms and a double sum running over all atoms of the crystal. The latter, however, will be shown to arise exclusively from the electrostatic interaction of point charges located at the atomic sites and can be identified with the Madelung energy as contained in Eq. (86). Hence we complement Eq. (86) with the results

$$E_{T,i} = \sum_{l\sigma}\left[\sum_{\alpha=1}^{2}\bar{E}_{li\sigma}^{(\alpha)}Q_{li\sigma}^{(\alpha)} + (2l+1)\sum_{n_i}\bar{E}_{lin_i}\right]$$
$$- \int_{\Omega_i}\int_{\Omega_i}d^3\mathbf{r}_i\,d^3\mathbf{r}'_i\frac{\rho_{\mathrm{el},i}(\mathbf{r}_i)\rho_{\mathrm{el},i}(\mathbf{r}'_i)}{|\mathbf{r}_i - \mathbf{r}'_i|}$$
$$+ \sum_\sigma\int_{\Omega_i}d^3\mathbf{r}_i\big[\varepsilon_{\mathrm{xc},i\sigma}(\mathbf{r}_i) - v_{\mathrm{xc},i\sigma}(\mathbf{r}_i)\big]\rho_{\mathrm{el},i\sigma}(\mathbf{r}_i) \quad (95)$$

and

$$E_{\mathrm{Mad}} = \frac{1}{2}\sum_i v_{\mathrm{Mad},i}Q_i + \frac{1}{2}\sum_j v_{\mathrm{Mad},j}Q_j$$
$$- \sum_\mu\sum_{ij}(1 - \delta_{\mu0}\delta_{ij})\frac{Q_iQ_j}{|\boldsymbol{\tau}_j - \boldsymbol{\tau}_i - \mathbf{R}_\mu|}$$
$$+ \sum_\mu\sum_{ij}(1 - \delta_{\mu0}\delta_{ij})\frac{Z_iZ_j}{|\boldsymbol{\tau}_j - \boldsymbol{\tau}_i - \mathbf{R}_\mu|}. \quad (96)$$

In the last step we have used the translational invariance of the lattice. Finally, using the definition (72) of the Madelung potential, we get the result for the Madelung energy,

$$E_{\mathrm{Mad}} = \sum_\mu\sum_{ij}(1 - \delta_{\mu0}\delta_{ij})\frac{(Q_i - Z_i)(Q_j - Z_j)}{|\boldsymbol{\tau}_j - \boldsymbol{\tau}_i - \mathbf{R}_\mu|}$$
$$= \frac{1}{2}\sum_i v_{\mathrm{Mad},i}(Q_i - Z_i), \quad (97)$$

which concludes our description of the standard ASW method.

The Electronic Structure of FeS$_2$

As an illustration of the capabilities offered by the augmented spherical wave method, we present some results of our recent work on iron pyrite [70, 71]. In general, the pyrite-type transition metal disulfides MS$_2$, with M = Fe, Co, Ni, Cu, Zn, Ru, have long attracted scientific and technological interest because of a broad range of electronic, magnetic, and optical properties (see, e.g., [72–78]). Among these compounds are semiconductors like the van Vleck paramagnet FeS$_2$ and the wide-band gap diamagnet ZnS$_2$. In contrast, CoS$_2$ is a ferromagnetic metal ($T_C \approx 130$ K) whereas CuS$_2$ becomes superconducting [73, 79–81]. Much interest has also been focused on the antiferromagnetic insulator NiS$_2$, which undergoes two magnetic phase transitions at $T_{N_1} \approx 54$ K and $T_{N_2} \approx 31$ K [73, 80–83], and has been interpreted in terms of the Mott–Hubbard-type picture for highly correlated electron systems [77, 81]. In general, the changing influence of electron correlations across the series, which is related to the successive filling of the e_g manifold of the crystal field split d bands, remains a central issue. A systematic study is favored by the fact that the sulfides from FeS$_2$ to CuS$_2$ and the selenides of Co and Ni form solid solutions [81, 84]. As a consequence, the occupation of the e_g band can be continuously varied, thus allowing for the construction of comprehensive phase diagrams [81].

Much interest has focused on iron pyrite FeS$_2$ for its promising capabilities as a material for photovoltaic applications [85]. This is, of course, related to its high quantum efficiency (>90%) and high absorption coefficient ($\geq 10^5$ cm^{-1} for $h\nu > 1.3$ eV), but also benefits from the nontoxity of the constituents [86, 87]. Yet, the rather small value of the optical band gap of 0.9–0.95 eV prohibits optimal use of the solar spectrum. For this reason, many studies have been aimed at increasing the band gap, e.g., by alloying with other materials.

Our investigation of FeS$_2$ was motivated by the recent observation of a considerable increase of the optical band gap (by about 0.07 eV) when only a very small amount ($< 5 \times 10^{20}$ cm^{-3}) of Zn was implanted into FeS$_2$ [71]. The absence of any indications of additional phases and the fact that Zn and Fe are frequently associated in minerals led us to conclude that the Zn atoms homogeneously sub-

stitute for Fe atoms. The aforementioned concentration then corresponds to a Zn content of $\approx 2\%$ and an average Zn–Zn distance of about 15 Å. In view of this small concentration, as well as the fact that ZnS$_2$ is a wide-gap semiconductor with 3d states located well below the valence band maximum, an explanation of this gap widening exclusively in terms of the electronic states seemed unlikely. Since Zn has a larger atomic radius as compared to iron, we proposed instead a mechanism based on crystal structure distortions caused by the incorporation of Zn impurities into iron pyrite and a considerable electron–lattice interaction [70]. The latter would transform the structural deviations into the observed changes of the electronic structure. To get more support for these ideas as well as to get, in general, deeper insight into the electronic structure of FeS$_2$, we initiated a comprehensive first-principles study.

CRYSTAL STRUCTURE

At room temperature, FeS$_2$ crystallizes in the pyrite structure, which is based on a simple cubic lattice with space group $Pa\bar{3}$ (T_h^6) [87–89] and lattice constant $a = 5.4160$ [89]. The crystal structure is displayed in Figure 2. The positions of the atoms and the crystal structure parameter are listed in Table I, where the Wyckoff positions (4a) and (8c) are special cases of the general position (24d): $\pm(x, y, z)$, $\pm(\frac{1}{2}-x, -y, \frac{1}{2}+z)$, $\pm(-x, \frac{1}{2}+y, \frac{1}{2}-z)$, $\pm(\frac{1}{2}+x, \frac{1}{2}-y, -z)$ (and cyclic permutations of x, y, and z).

The pyrite crystal structure is best described in terms of the NaCl structure with the sublattices
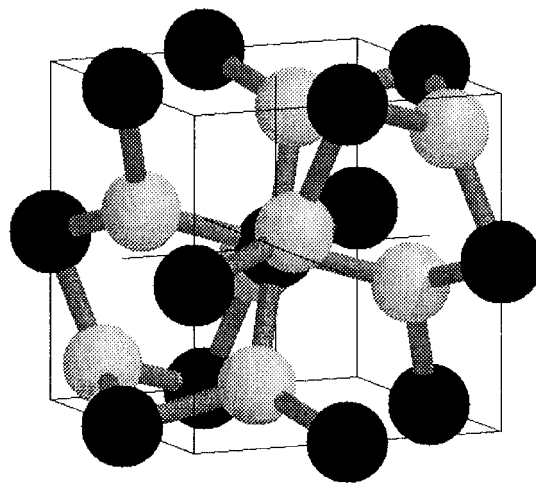
FIGURE 2. Crystal structure of FeS$_2$. Iron and sulfur atoms are printed in black and light gray, respectively.

Crystal structure parameters of pyrite FeS$_2$ (from Ref. [89]).

Atom	Wyckoff positions	Parameter x
Fe	(4a)	
S	(8c)	0.38484

occupied by iron atoms and the centers of gravity of sulfur atom pairs, respectively. These sulfur dumbbells are oriented along the ⟨111⟩ axes. Their bond length of 2.161 Å is still shorter than the Fe–S distance of 2.265 Å. While the sulfur atoms are tetrahedrally coordinated by one sulfur and three iron atoms, the six nearest neighbor sulfur atoms at each iron site form slightly distorted octahedra. Due to the deformations of the octahedra, the local symmetry at these sites is reduced from cubic (O_h) to trigonal (C_{3i}). The distorted FeS$_6$ octahedra are interlinked by common corners and, due to the formation of the ⟨111⟩ sulfur pairs, have rotated away from the Cartesian axes by about 23°. For a two-dimensional crystal, the situation is sketched in Figure 3. Obviously, the formation of the ⟨111⟩ sulfur pairs does not destroy the square planar coordination of the iron atoms. Instead, the squares built by the sulfur atoms just shrink and rotate. Since the orientation of the dumbbells conforms with the cubic point group, the underlying Bravais lattice is no longer face-centered, but simple cubic, and the unit
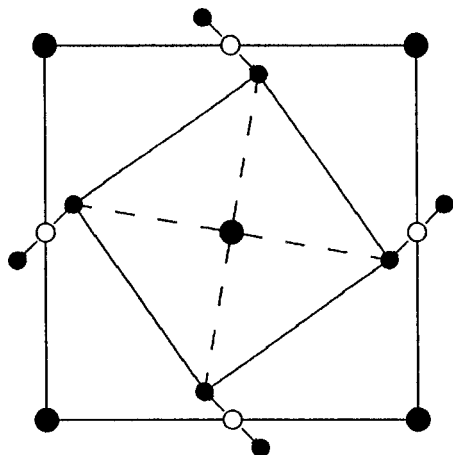
FIGURE 4. First Brillouin zone of the simple cubic lattice.

cell comprises four formula units. Yet, as we will see below, some features of the electronic structure may still be understood in terms of the face-centered cubic (fcc) lattice.

According to Bradley and Cracknell the space group $Pa\bar{3}$ (T_h^6) is exceptional among the 230 space groups because it is the only one that is neither an invariant subgroup of a larger space group based on the simple cubic Bravais lattice nor a member of a pair of isomorphic space groups [90]. For this reason, the irreducible wedge of the first Brillouin zone as given in Figure 4 is twice as big as that of the more familiar monoatomic case and we have to distinguish the high symmetry points $X = (0, \frac{1}{2}, 0)$ and $X' = (\frac{1}{2}, 0, 0)$.

COMPUTATIONAL ASPECTS

As already discussed, the open structure of FeS$_2$ calls for inclusion of empty spheres to model the full crystal potential and to minimize the overlap of the atomic spheres. We used the aforementioned sphere geometry optimization algorithm [27] to find optimal empty sphere positions as well as radii of all spheres. As a result, by inserting 32 empty spheres into the simple cubic unit cell of FeS$_2$, we were able to keep the linear overlap of any two physical spheres below 10% and the overlap of any pair of physical and empty spheres below 18%. The positions of the empty spheres are listed in Table II. In addition to the empty sphere positions, the algorithm proposed the following sphere radii: Fe, 2.243a_B; S, 2.223a_B; E$_1$, 1.630a_B; E$_2$, 1.543a_B.

The basis set used for the present calculations comprises Fe 4s, 4p, and 3d orbitals, S 3s, 3p, and 3d orbitals, and 1s, 2p orbitals of the empty

FIGURE 3. Two-dimensional analogue of the pyrite structure. Large and small filled circles designate iron and sulfur atoms, respectively. Small open circles mark the ideal positions of the rock salt structure.

TABLE II
Empty sphere positions for pyrite FeS$_2$.

Atom	Wyckoff positions	Parameters		
		x	y	z
E$_1$	(8c)	0.1935		
E$_2$	(24d)	0.4446	0.1373	0.1980

spheres. In addition, 4f states of Fe and S as well as empty sphere 3d states were included as intermediate waves, hence, as tails of the aforementioned orbitals. Finally, the Brillouin zone sampling was done using an increasing number of **k** points, which range from 11, 24, 76 to 176 points within the irreducible wedge.

CALCULATIONS USING THE EXPERIMENTAL CRYSTAL STRUCTURE

To first approximation, the electronic structure of FeS$_2$ may be discussed in terms of a molecular orbital picture, where the formation of $(S_2)^{2-}$ pairs leads to five occupied sulfur states per pair. In contrast, the remaining antibonding $p\sigma^*$ band will be located above the insulating gap. Accordingly, iron turns out to be in a $3d^6$ configuration and has a low spin $(t_{2g})^6(e_g)^0$ state in octahedral coordination. Since the distortion of the FeS$_6$ octahedral lowers the symmetry of the crystal field at the iron site from cubic (O_h) to trigonal (C_{3i}), the t_{2g} levels are further split into a low lying twofold degenerate e_g^π level and a higher a_{1g} singlet [91, 92]; for clarity the original e_g level is then designated as the e_g^σ state. Nevertheless, since the deviations from octahedral symmetry are rather small, we still expect that the crystal field splitting is dominated by its cubic part.

We show in Figure 5 the calculated band structure of FeS$_2$ along selected high symmetry lines within the first Brillouin zone of the simple cubic lattice, Figure 4. The corresponding dominant partial densities of states. (DOS) per formula unit are given in Figure 6. All other states of Fe and S that are not included in Figure 6 play only a negligible role in the given energy interval. To account for the aforementioned nearly cubic crystal field splitting, we have furthermore split the Fe 3d partial DOS into the t_{2g} and e_g manifolds. Note, however, that, due to the tilting of the FeS$_6$ octahedra by 23°, we had to rotate the frame of reference before performing the projection onto the partial 3d states.
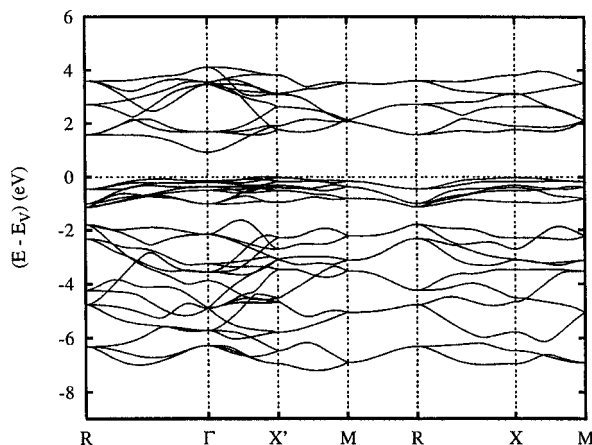
FIGURE 5. Electronic bands of FeS$_2$ along selected symmetry lines within the first Brillouin zone of the simple cubic lattice, Figure 4. Here and in the following figures, energies are given relative to the valence band maximum E_V.

In Figures 5 and 6 we identify three groups of bands. In the energy range from -7.3 to -1.5 eV we find a group of 20 bands that derive from hybridized Fe 3d and S 3p orbitals with larger contributions from the latter. Bands are most easily counted along the line M–R, where they are fourfold degenerate. Just below the valence band maximum a group of 12 bands appears, which originates mainly from iron 3d t_{2g} states with a small admixture from sulfur 3p states. In the following discussion we will designate these two groups of bands as the lower and upper valence bands, respectively. The conduction band likewise comprises 12 bands.
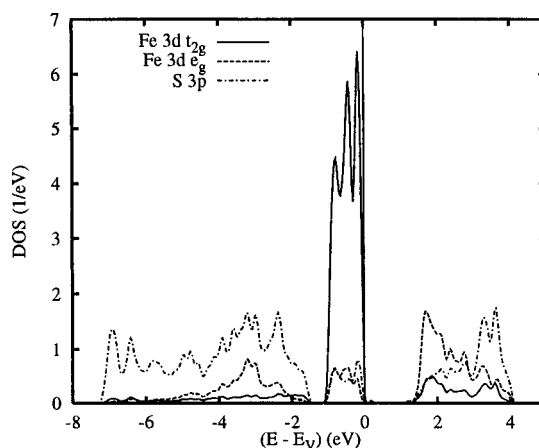
FIGURE 6. Partial densities of states (DOS) of FeS$_2$ per formula unit. The selection of orbitals is relative to a rotated reference frame (see text).
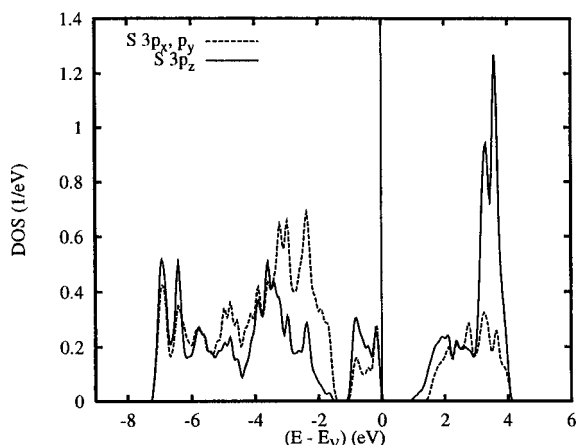
FIGURE 7. Partial S 3p densities of states (DOS) of FeS_2. The selection of orbitals is relative to a rotated reference frame (see text).

They are of Fe 3d e_g and S 3p character with the relative contributions gradually changing as the energy increases. In particular, the S 3p states show up in the pronounced double peak at ≈ 3.5 eV. While the t_{2g} bands appear mainly in the upper valence band without any substantial bonding–antibonding splitting, the e_g levels, which, forming σ bonds, have a much larger overlap with the S 3p orbitals, experience a considerable splitting into bonding and antibonding states with the main peaks at ≈ -3.5 and 2 eV, respectively. The indirect optical band gap separating occupied and unoccupied states amounts to ≈ 0.95 eV, which is in very good agreement with the experimental values ranging from 0.9 to 0.95 eV as deduced from optical and conductivity measurements [85]. From the band structure as well as from a scan through the first Brillouin zone on a mesh of $30 \times 30 \times 30$ points we are able to locate the valence

band maximum at the point (0.0, 0.0, 0.4136), hence, in the vicinity of the X point. In contrast, the conduction band minimum is found at the Γ point.

The partial densities of states arising from the single 3p components of those two sulfur atoms, which are near the center of the cubic unit cell, are shown in Figure 7, where we have now rotated the frame of reference such that the local z axis lies parallel to the $\langle 111 \rangle$ line connecting both sulfur atoms. The $3p_z$ partial DOS show distinct deviations from the $3p_x$ and $3p_y$ curves and, in particular, dominate the unoccupied, hence, antibonding S 3p states. This becomes obvious from the characteristic double peak of the $3p_z$ DOS at about 3.5 eV. The bonding counterpart is found at -6.75 eV, whereas the $3p_x$ and $3p_y$ curves dominate in the energy range between ≈ -4 and ≈ -1.5 eV. Hence, among the three sulfur 3p bands, the p_z, states show the largest bonding–antibonding splitting. This is not suprising since the $3p_z$ states form σ bonds between the two sulfur atoms of a pair, whereas the $3p_x$ and $3p_y$ orbitals experience a much smaller overlap via S—S π bonds. However, the lowest edge of the conduction band is still exclusively due to the $3p_z$ orbitals without any contributions from the other two 3p or the Fe 3d e_g orbitals. This fact becomes even more obvious from Figure 8, where we display the near-gap electronic bands in a special representation. In both parts of this figure, each band at each **k** point is given a bar, the length of which is a measure of the contribution from a specified orbital. In particular, we observe a dominating influence of the Fe 3d states to the upper valence band, while these bands have no bars indicative of S 3p states. For the conduction bands we observe strong Fe 3d contributions in the energy window from ≈ 1.5 to 3.0 eV, whereas for energies above this range and especially at the lowest edge of
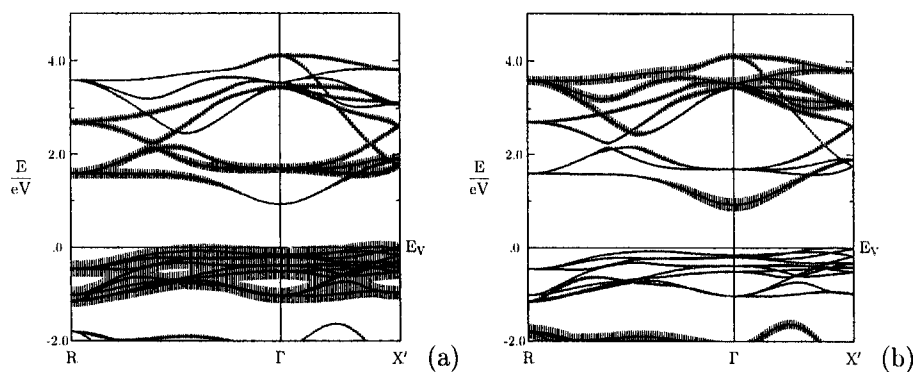
FIGURE 8. Weighted electronic bands of FeS_2. The width of the bars given for each band indicates the contribution due to the (a) Fe 3d and (b) S 3p orbitals, respectively.

the conduction bands, S 3p dominate. The change of band character from Fe 3d to S 3p can be clearly observed in the lowest conduction band along the line R–Γ. At Γ this band is exclusively due to S 3p states, but due to hybridization with the Fe 3d states, it changes character on the way to the R point. In the middle between both points the band at 2.5 eV takes over the S 3p character and keeps it until the R point is reached at about 3.7 eV. From a different point of view we interpret the band starting at Γ at ≈ 1.0 eV and dispersing almost linearly to 3.7 eV at the R point as the S 3p band, which hybridizes with the dispersionless e_g bands in the energy region between 1.5 and 2.5 eV, half way between Γ and R. The situation is not unlike that in elementary Cu, where the lowest s-like band hybridizes with the 3d states just below the Fermi energy but again assumes the original 4s character above E_F [24]. Finally, we arrive at the rather surprising conclusion that the optical band gap separates Fe 3d t_{2g} and S 3p$_z$ orbitals and, hence, although it is strongly influenced by the crystal field splitting, cannot be described exclusively in terms of it. In contrast, the different orbital compositions of the valence band maximum and the conduction band minimum provide a natural explanation for the high optical absorption.

ROLE OF CRYSTALLINE DISTORTIONS

We have still not yet paid much attention to the factors that might influence the optical band gap. Indeed, it would be desirable to identify mechanisms that change the size or the indirect nature of the gap or modify the composition of the near-gap states. More insight into such mechanisms would finally allow us to address the question of why incorporation of small amounts of Zn into FeS$_2$ leads to the experimentally observed widening of the optical band gap [71].

Since it is unlikely that the changes of the electronic structure of FeS$_2$ when Zn is substituted for Fe can be explained solely from the differences in the electronic configurations we studied, in particular, the sensitivity of the electronic structure to symmetry conserving deviations from the measured crystal structure. Obviously, such an investigation not only serves as a necessary prerequisite for a solution of the aforementioned problem, but is an interesting topic in itself.

In a first step, we simulated the application of external pressure by performing a fully self-consistent calculation with the lattice constant reduced by 5%. As a result, there are two main effects: (i) Hydrosta-

tic pressure leads to a broadening of all bands without noticeable reorderings of the electronic states. At the same time, there is a corresponding reduction of the total and partial DOS. (ii) The main peaks of the lower valence and the conduction band experience rather large shifts to lower and higher energies, respectively. For the lowest and highest peaks, the shifts are even as large as about 1 eV. In particular, the pronounced S 3p$_z$ dominated double peaks at about -6.75 and 3.5 eV move to ≈ -7.5 and ≈ 4.4 eV, respectively. These findings can be understood from the fact that application of isotropic pressure increases both the crystal field and the bonding–antibonding splitting of the bands and thus leads to an overall spreading of the band structure. Nevertheless, since the resulting band shifts add to the aforementioned band broadenings, the size of the optical band gap remains essentially unchanged.

The situation is different when the internal sulfur x parameter is varied. We performed fully self-consistent calculations using the (hypothetical) values $x_- = 0.38084$ and $x_+ = 0.38884$, respectively. As a result, we observed a large shift of the optical band gap of about 0.67 eV on going from x_- to x_+, hence, moving the sulfur atoms by less than 1% of the lattice constant. This change of the band gap is due to a large shift of the conduction band minimum (CBM) relative to the centers of gravity of both the valence and conduction band, which stay essentially inert. There is, however, a noticeable shift of the sulfur 3p$_z$ dominated double peak at about 3.5 eV, which moves by approximately 0.5 eV. As a consequence, the total width of the conduction band is reduced.

Variation of the x parameter thus almost entirely affects the S 3p, especially the 3p$_z$ states. Their response to the changes of the crystal structure is twofold: (i) An increase of the sulfur x parameter leads to a closer coupling of the sulfur pairs and, hence, to a larger bonding–antibonding splitting. This is revealed by the shifts of the 3p$_z$ double peaks. (ii) The increase of the x parameter, while shortening the sulfur–sulfur bonds, reduces the hopping across the lattice. For this reason the dispersion of both the S 3p$_z$ bonding and antibonding bands decreases, which causes the upshift of the CBM. The sulfur sublattice should thus be discussed in terms of a molecular S$_2$ crystal.

Finally, we are able to sketch a scenario for the substitution of Zn atoms for Fe: Due to the larger atomic radius of Zn as compared to Fe, each Zn impurity will push apart its six nearest neighbor sulfur atoms. Since, as known from Raman exper-

iments [93], the S—S bond is rather soft, this causes a compression of the S_2 molecules and thus the just outlined strong upshift of the antibonding S $3p_z$, bands. In addition, since the sulfur states at the lower edge of the conduction band arise from dispersion across the simple cubic lattice, they are strongly affected by only small disturbances of the crystal structure. Hence, we expect a strong shift of the conduction band minimum already for a small amount of Zn impurities, which is indeed observed in experiment.

Conclusion

The central issue of the present contribution was a description of modern schemes for electronic structure calculations with the augmented spherical wave (ASW) method. To lay ground for a thorough understanding of the formalism, we started out with a short review of the basics of modern band theory as well as the most important methods for electronic structure calculations currently in use. In doing so, we emphasized the fundamental ideas common to most methods and reduced the differences between them to different idealizations of the single-particle potential used for the construction of basis functions (pseudopotential, muffin-tin approximation) as well as to the size of the basis set needed for an accurate prescription of the wave function.

The description of the ASW method itself ranged from the explicit construction of the basis functions to the calculation of the density of states, the charge density, the effective potential, and the total energy, all of which contribute to the comprehensive understanding of material properties. This included a discussion of the influence of approximations underlying the method, for instance, the muffin-tin or the atomic sphere approximation. The theoretical derivations were complemented by discussions of the practical aspects of the method with respect to both implementation and application.

Finally, the theoretical part was followed by a discussion of our recent results on FeS_2, which served the purpose of illustrating the predictive power of modern band theory. In particular, from a detailed analysis of the electronic states by means of partial densities of states and orbital weighted band structures, we were able to identify the relevant orbitals. Their sensitivity to changes of the crystal structure was revealed by additional calculations with hypothetically distorted structures. Eventually, we were able to propose an explanation for the recently observed widening of the optical band gap on the incorporation of only small amounts of Zn.

References

1. Bloch, F. Z Phys 1929, 52, 555.
2. Born, M.; Oppenheimer, R. Ann Phys (Leipzig) 1927, 84, 457.
3. Slater, J. C. Phys Rev 1937, 51, 846.
4. Hohenberg, P.; Kohn, W. Phys Rev 1964, 136, B864.
5. Kohn, W.; Sham, L. J. Phys Rev 1965, 140, A1133.
6. Kohn, W.; Vashishta, P. In Theory of the Inhomogeneous Electron Gas; Lundqvist, S.; March, N. H., Ed.; Plenum: New York, 1983; pp. 79–147.
7. von Barth, U. In The Electronic Structure of Complex Systems; Phariseau, P.; Temmerman, W., Eds.; Plenum: New York, 1984; pp. 67–140.
8. Williams, A. R.; von Barth, U. In Theory of the Inhomogeneous Electron Gas; Lundqvist, S.; March, N. H., Eds.; Plenum: New York, 1983; pp. 189–307.
9. Dreizler, R. M.; de Providência, J., Eds. Density Functional Methods in Physics; Plenum: New York, 1985.
10. Dreizler, R. M.; Gross, E. K. U. Density Functional Theory; Springer: Berlin, 1990.
11. Kryachko, E. S.; Ludeña, E. V. Energy Density Functional Theory of Many-Electron Systems; Kluwer Academic: Dordrecht, 1990.
12. von Barth, U. In Methods of Electronic Structure Calculations; Kumar, V.; Andersen, O. K.; Mookerjee, A., Eds.; World Scientific: Singapore, 1994; pp. 21–62.
13. Gross, E. K. U.; Dreizler, R. M., Eds. Density Functional Theory; Plenum: New York, 1995.
14. Eschrig, H. The Fundamentals of Density Functional Theory; Teubner: Stuttgart, 1996.
15. Herring, C. Phys Rev 1940, 57, 1169.
16. Phillips, J. C.; Kleinman, L. Phys Rev 1959, 116, 287.
17. Antoncik, E. J Phys Chem Solids 1959, 10, 314.
18. Andersen, O. K. Solid State Commun 1973, 13, 133.
19. Andersen, O. K. Phys Rev B 1975, 12, 3060.
20. Car, R.; Parrinello, M. Phys Rev Lett 1985, 55, 2471.
21. Williams, A. R.; Kübler, J.; Gelatt, C. D., Jr. Phys Rev B 1979, 19, 6094.

22. Kübler, J.; Eyert, V. In Electronic and Magnetic Properties of Metals and Ceramics; Buschow, K. H. J., Ed.; VCH Verlagsgesellschaft: Weinheim, 1992; pp. 1–145. Cahn, R. W.; Haasen, P.; Kramer, E. J., Eds. Materials Science and Technology; VCH Verlagsgesellschaft: Weinheim, 1991–1996; Vol. 3A.

23. Eyert, V. Ph.D. Thesis, Technische Hochschule Darmstadt, 1991.

24. Eyert, V. In Density Functional Methods: Applications in Chemistry and Materials Science; Springborg, M., Ed.; Wiley: Chichester, 1997; pp. 233–304.

25. Eyert, V. Octahedral Deformations and Metal-Insulator Transition in Transition Metal Chalcogenides, Habilitation Thesis, Universität Augsburg, 1998.

26. Eyert, V. J Comput Phys 1996, 124, 271.

27. Eyert, V.; Höck, K.-H. Phys Rev B 1998, 57, 12,727.

28. Matar, S. F. Int J Quant Chem 1999, 00, 000, this volume.

29. Heine, V. In Solid State Physics; Ehrenreich, H.; Seitz, F.; Turnbull, D., Eds.; Academic Press: Orlando, FL, 1970; Vol. 24, pp. 1–36.

30. Callaway, J. Energy Band Theory; Academic Press: New York, 1964.

31. Callaway, J. Quantum Theory of the Solid State; Academic Press: New York, 1974.

32. Phillips, J. C. Phys Rev 1958, 112, 685.

33. Hamann, D. R. Phys Rev Lett 1979, 42, 662.

34. Hamann, D. R. Phys Rev B 1989, 40, 2980.

35. Bachelet, G. B.; Hamann, D. R.; Schlüter, M. Phys Rev B 1982, 26, 4199.

36. Vanderbilt, D. Phys Rev B 1990, 41, 7892.

37. Cohen, M. L. Phys Rep 1984, 110, 293.

38. Cohen, M. L.; Heine, V. In Solid State Physics; Ehrenreich, H.; Seitz, F.; Turnbull, D., Eds.; Academic Press: Orlando, FL, 1970; Vol. 24, pp. 37–248.

39. Austin, B. J.; Heine, V.; Sham, L. J. Phys Rev 1962, 127, 276.

40. Slater, J. C. Quantum Theory of Molecules and Solids; McGraw-Hill: New York, 1965; Vol. 2.

41. Loucks, T. Augmented Plane Wave Method; Benjamin: New York, 1967.

42. Korringa, J. Physica 1947, 13, 392.

43. Kohn, W.; Rostoker, N. Phys Rev 1954, 94, 1111.

44. Williams, A. R. Phys Rev B 1970, 1, 3417.

45. Williams, A. R.; van W. Morgan, J. J Phys C 1974, 7, 37.

46. Segall, B.; Ham, F. S. In Methods in Computational Physics; Alder, B.; Fernbach, S.; Rotenberg, M., Eds.; Academic Press: New York, 1968; pp. 251–293.

47. Andersen, O. K. In The Electronic Structure of Complex Systems; Phariseau, P.; Temmerman, W., Eds.; Plenum: New York, 1984; pp. 11–66.

48. Andersen, O. K.; Jepsen, O.; Glötzel, D. In Highlights of Condensed-Matter Theory. Proceedings of the International School of Physics "Enrico Fermi," Course LXXXIX. Bassani, F.; Fumi, F.; Tosi, M. P., Eds.; North-Holland: Amsterdam, 1985; pp. 59–176.

49. Andersen, O. K.; Jepsen, O.; Sob, M. In Electronic Band Structure and Its Applications; Yussouff, M., Ed.; Springer: Berlin, 1986; pp. 1–57.

50. Andersen, O. K.; Postnikov, A. P.; Savrasov, S. Yu. Mater Res Soc Symp Proc 1992, 253, 37.

51. Singh, D. J. Planewaves, Pseudopotentials and the LAPW Method; Kluwer Academic: Boston, 1994.

52. Skriver, H. L. The LMTO Method; Springer: Berlin, 1984.

53. Watson, R. E.; Ehrenreich, H.; Hodges, L. Phys Rev Lett 1970, 15, 829.

54. Hodges, L.; Watson, R. E.; Ehrenreich, H. Phys Rev B 1972, 5, 3953.

55. Gelatt, C. D., Jr.; Ehrenreich, H.; Watson, R. E. Phys Rev B 1977, 15, 1613.

56. Wang, C. S.; Callaway, J. Comput Phys Commun 1978, 14, 327.

57. Eschrig, H. Optimized LCAO Method and the Electronic Structure of Extended Systems; Springer: Berlin, 1989.

58. Payne, M. C.; Teter, M. P.; Allan, D. C.; Arias, T. A.; Joannopoulos, J. D. Rev Mod Phys 1992, 64, 1045.

59. Terakura, K. In Computational Physics as a New Frontier in Condensed Matter Research; Takayama, H.; Tsukuda, M.; Shiba, H.; Yonezawa, F.; Imada, M.; Okabe, Y., Eds.; The Physical Society of Japan, Tokyo, 1995.

60. Abramowitz, M.; Stegun, I. A. Handbook of Mathematical Functions; Dover: New York, 1972.

61. von Barth, U. In Many-Body Phenomena at Surfaces; Langreth, D.; Suhl, H., Eds.; Academic Press: Orlando, 1984; pp. 3–50.

62. Jackson, J. D. Chemical Electrodynamics; Wiley: New York, 1975.

63. Fuller, E. R.; Naimon, E. R. Phys Rev B 1972, 6, 3609.

64. Sholl, C. A. Proc Phys Soc 1967, 92, 434.

65. Mattheiss, L. F. Phys Rev 1964, 133, A1399.

66. Jepsen, O.; Andersen, O. K. Z Phys B 1995, 97, 35.

67. Hedin, L.; Lundqvist, B. I. J Phys C 1971, 4, 2064.

68. Moruzzi, V. L.; Janak, J. F.; Williams, A. R. Calculated Electronic Properties of Metals; Pergamon Press: New York, 1978.

69. von Barth, U.; Hedin, L. J Phys C 1972, 5, 1629.

70. Eyert, V.; Höck, K.-H.; Fiechter, S.; Tributsch, H. Phys Rev B 1998, 57, 6350.

71. Büker, K.; Fiechter, S.; Eyert, V.; Tributsch, H. J Electrochem Soc 1999, 146, 261.

72. Munson, R. A.; DeSorbo, W.; Kouvel, J. S. J Chem Phys 1967, 47, 1769.

73. Bither, T. A.; Bouchard, R. J.; Cloud, W. H.; Donohue, P. C.; Siemons, W. J. Inorg Chem 1968, 7, 2208.

74. Jarrett, H. S.; Cloud, W. H.; Bouchard, R. J.; Butler, S. R.; Frederick, C. G.; Gillson, J. L. Phys Rev Lett 1968, 21, 617.

75. Wilson, J. A.; Yoffe, A. D. Adv Phys 1969, 18, 193.

76. Wilson, J. A.; Pitt, G. D. Philos Mag 1971, 23, 1297.

77. Ogawa, S.; Waki, S.; Teranishi, T. Int J Magn 1974, 5, 349.

78. Kikuchi, K.; Miyadai, T.; Itoh, H.; Fukui, T. J Phys Soc Jpn 1978, 45, 444.

79. Miyahara, S.; Teranishi, T. J Appl Phys 1968, 39, 896.

80. Adachi, K.; Sato, K.; Yamanchi, K.; Ohashi, M. J Phys Soc Jpn 1972, 32, 573.

81. Ogawa, S. J Appl Phys 1979, 50, 2308.

82. Hastings, J. M.; Corliss, L. M. IBM J Res Dev 1970, 14, 227.

83. Miyadai, T.; Kikuchi, K.; Ito, Y. Physica B 1977, 86–88, 901.

84. Yao, X.; Kuo, Y.-K.; Powell, D. K.; Brill, J. W.; Honig, J. M. Phys Rev B 1997, 56, 7129.

85. Ennaoui, A.; Fiechter, S.; Pettenkofer, Ch.; Alonso-Vante, N.; Büker, K.; Bronold, M.; Höpfner, Ch.; Tributsch, H. Sol Energy Mater Sol Cells 1993, 29, 289.

86. Ennaoui, A.; Fiechter, S.; Jaegermann, W.; Tributsch, H. J Electrochem Soc 1986, 133, 97.

87. Birkholz, M.; Fiechter, S.; Hartmann, A.; Tributsch, H. Phys Rev B 1991, 43, 11,926.

88. Finklea, S. L., III; Cathey, L.; Amma, E. L. Acta Crystallogr 1976, 32, 529.

89. Stevens, E. D.; DeLucia, M. L.; Coppens, P. Inorg Chem 1980, 19, 813.

90. Bradley, C. J.; Cracknell, A. P. The Mathematical Theory of Symmetry in Solids; Clarendon Press: Oxford, 1972.

91. Goodenough, J. B. J Solid State Chem 1971, 3, 26.

92. Goodenough, J. B. J Solid State Chem 1972, 5, 144.

93. Sourisseau, C.; Cavagnat, R.; Fouassier, M. J Phys Chem Solids 1991, 52, 537.